

The dynamics of carbon cycle changes and their underlying mechanisms during the Sakmarian to Artinskian transition

Yanan Li ^{a,b,*}, Longyi Shao ^c, Christopher R. Fielding ^d, Tracy D. Frank ^d, Zhaorui Ye ^e, Jing Lu ^c, Kuan Yang ^a, Shuai Wang ^{a,b}

^a Department of Geological Sciences and Engineering, College of Mining, Liaoning Technical University, Fuxin, Liaoning 123000, People's Republic of China

^b Liaoning Key Laboratory of Green Development of Mineral Resources, Liaoning Technical University, Fuxin, Liaoning 123000, People's Republic of China

^c State Key Laboratory for Fine Exploration and Intelligent Development of Coal Resources and College of Geoscience and Surveying Engineering, China University of Mining and Technology (Beijing), D11 Xueyuan Road, Beijing 100083, People's Republic of China

^d Department of Earth Sciences, University of Connecticut, Storrs, CT 06269, USA

^e New energy geological team of Hebei Coalfield Geological Bureau, Xingtai, Hebei 054000, People's Republic of China

ARTICLE INFO

Editor: H. Falcon-Lang

Keywords:

Volcanic activity

Deglaciation

Carbon cycle

Paleoclimate

Late Paleozoic Ice Age

ABSTRACT

The Sakmarian to Artinskian transition was marked by significant global climate change, evolving from glacial to postglacial conditions in high southern paleolatitudes. This climate transformation was accompanied by significant paleoenvironmental changes, concomitant with a realignment in biodiversity patterns. Most previous studies attributed this climatic transition to increasing atmospheric $p\text{CO}_2$ concentrations, but the driving mechanisms during this period have not been clearly elucidated. To address these shortcomings, an integrated multi-proxy analysis was conducted, including measurements of mercury (Hg) and nickel (Ni) concentrations, total organic carbon (TOC), and carbon isotopic compositions of organic matter ($\delta^{13}\text{C}_{\text{org}}$) on a Sakmarian to Artinskian succession in North China. This investigation was carried out within the context of a new U-Pb zircon age-constrained framework, ranging from 295.6 ± 0.1 Ma to 284.2 ± 2.4 Ma, which covers the interval from the Shansi Formation to the Lower Shihhotse Formation in the Dacheng coalfield, Hebei Province. Simultaneous late Sakmarian Hg and Hg/TOC peaks, temporally coupled with negative $\delta^{13}\text{C}_{\text{org}}$ excursions and dated tuffaceous mudstone layers, demonstrate that elevated Hg levels and carbon cycle perturbations were primarily driven by volcanic activity, with wildfires as a secondary contributor. Volcanic activity potentially associated with the Tarim II Large Igneous Province likely played a role in elevating atmospheric $p\text{CO}_2$ concentrations around the Sakmarian-Artinskian boundary, which may have triggered the nonglacial interval that separated the P1 and P2 glaciations. Sustained elevated atmospheric $p\text{CO}_2$ during the earliest Artinskian stage might be additionally attributed to the contraction of tropical coal-forming forests, an emerging trend towards more arid climates, and increased wildfires. Results offer insights into the interplay among volcanic forcing, terrestrial feedbacks, glaciations, climate dynamics, and carbon cycle disturbances during this critical phase of the late Paleozoic Ice Age.

1. Introduction

The late Paleozoic Ice Age (LPIA; ca. 360–254.5 Ma) was the only known prolonged climate transition from icehouse to greenhouse conditions on vegetated Earth (Crowell, 1978; Veevers and Powell, 1987; Isbell et al., 2003; Montañez et al., 2007; Isbell et al., 2021; Rosa and Isbell, 2021). The LPIA encompassed multiple climate shifts and eustatic sea-level change signals in far-field, low-latitude regions (Ross and Ross, 1987; Heckel, 1994; Martino, 2004; Rygel et al., 2008; Tabor and

Poulsen, 2008; Eros et al., 2012; Koch and Frank, 2012; Shao et al., 2014; Opluštil et al., 2016; Lu et al., 2021a; Lv et al., 2022; Li et al., 2023) that correspond to the expansion and retreat of ice-sheets in the near-field, middle to high-latitude regions of Gondwana (Crowell, 1978; Veevers and Powell, 1987; Isbell et al., 2003; Fielding et al., 2008; Metcalfe et al., 2015; Griffis et al., 2019, 2021; Fielding et al., 2023). During the Cisuralian, a global climate change is documented from the Sakmarian to Artinskian stages, marking a transition from a glacial to a postglacial state (Yang et al., 2014, 2016; Fielding et al., 2023). This

* Corresponding author at: Department of Geological Sciences and Engineering, College of Mining, Liaoning Technical University, Fuxin, Liaoning 123000, People's Republic of China.

E-mail address: yananli2012@sina.com (Y. Li).

climate transition was accompanied by a rise in chemical weathering intensity and an elevation of land surface temperatures (Goldberg and Humayun, 2010; Yang et al., 2014; Sun et al., 2022a), a dramatic rise in sea-level (Miller et al., 2005; Haq and Schutter, 2008; Ma et al., 2023), an increase in atmospheric $p\text{CO}_2$ concentrations (Montañez et al., 2007; Richey et al., 2020), a decline in peat-forming forest area (Cleal and Thomas, 2005) and coal deposits within paleotropical zones (Zhang et al., 1999; Wang, 2010), and the Artinskian warming event recognized in the Euramerican domain (Marchetti et al., 2022).

More recently, volcanic activity has been recognized as a significant mechanism for the release of greenhouse gases, which can lead to an increase in surface temperatures and ultimately bring about the cessation of glacial intervals, a phenomenon particularly pronounced during the Permian period (Chen and Xu, 2019; Lu et al., 2021b; Fielding et al., 2023; Wang et al., 2023). Volcanic activity also has the potential to inject high concentrations of metals into the Earth's atmosphere (Grasby et al., 2013, 2015; Burgess and Bowring, 2015; Percival et al., 2017). Hg concentrations have been widely used as a proxy to document volcanic activity within the sedimentary records of different geological ages (Nriagu and Becker, 2003; Pyle and Mather, 2003; Sanei et al., 2012; Sial et al., 2013; Amos et al., 2014; Percival et al., 2015; Grasby et al., 2019; Yager et al., 2021; Shen et al., 2023). Nickel anomalies have also been extensively utilized in geological investigations to implicate volcanic activity, particularly in sections of Permian-Triassic boundary (Kaiho et al., 2001; Rampino et al., 2002; Rothman et al., 2014; Fielding et al., 2019; Zhang et al., 2023). Other metals, such as Vanadium (V), Cobalt (Co), and Molybdenum (Mo), which may exhibit elevated accumulation rates, can similarly be considered as diagnostic markers for large-scale volcanic activity (Grasby et al., 2019). However, it is evident that not all LIP volcanism emits toxic metals, as noted by Percival et al. (2018) and Jones et al. (2019). This is attributed to the fact that certain LIPs lack the necessary eruptive mechanisms to effectively inject metals and other key climate-forcing aerosols into the stratosphere, which is essential for their widespread dispersion across the globe (Bryan, 2021). Additionally, some LIP events release considerably lower amounts of CO_2 , a reflection of the inherent complexities associated with LIP occurrences (Bryan, 2021). As such, there is pronounced variability among LIPs, with only some having the capacity to impact paleoclimate. The predominant reservoir of Hg in terrestrial ecosystems is found in soils, where it is associated predominantly with organic matter (Shen et al., 2022b). As such, it is crucial to consider the impact of surface organic matter combustion, such as wildfires, and soil erosion, since these processes can also lead to anomalies in Hg concentrations (Blum et al., 2014; Thibodeau et al., 2016; Shen et al., 2022b).

Although a robust paleotropical sedimentary record of the LPIA is present in North China (Li et al., 2021), the limited occurrence of limestone within the Cisuralian strata has posed challenges to the construction of carbonate isotopic records. However, the Cisuralian sedimentary succession in North China contains numerous intervals rich in organic matter, which facilitate the construction of a carbon isotope composition curve using bulk organic matter ($\delta^{13}\text{C}_{\text{org}}$). The $\delta^{13}\text{C}_{\text{org}}$ record offers a means of capturing fluctuations in atmospheric CO_2 levels and can be used to infer variations in the global carbon cycle (Faure et al., 1995; Wang, 2010; Vervoort et al., 2019).

The objectives of this study are to (1) establish a stratigraphic framework for the Sakmarian to Artinskian intervals in the Dacheng coalfield, North China, utilizing newly acquired U-Pb zircon dating results; (2) track stratigraphic changes in mercury (Hg) and nickel (Ni) concentrations, complemented by additional metal-based volcanic indicators, and to detect perturbations in the carbon cycle using $\delta^{13}\text{C}_{\text{org}}$ data, and (3) investigate the underlying mechanisms driving changes in atmospheric $p\text{CO}_2$, as well as the climate transition from a glacial to a postglacial state and the resultant environmental changes.

2. Geological setting

During the Cisuralian, North China was situated in a low-latitude zone ranging from 20 to 30°N, whereas the various Gondwana Basins were located in the mid- to high- paleolatitudes of the Southern Hemisphere (Fig. 1A; Scotese, 2014). The Cisuralian sedimentary deposits within the North China Basin were derived primarily from the uplifted regions of what is now northern Inner Mongolia (Zhang et al., 2014; Fig. 1B). During the deposition of the Shansi and Lower Shihhotse formations, the northern region of North China was characterized by deltaic to alluvial plain depositional environments (Fig. 1B and Table 1; Shao et al., 2014; Li et al., 2021; Shao et al., 2024).

The stratigraphic succession of the Shansi and Lower Shihhotse formations in North China is continuous, with no evidence of hiatuses. Within the Dacheng coalfield, the Shansi Formation is noted for its multiple depositional cycles (Fig. 2). Each depositional cycle initiates with 1–8 m thick, fining-upward succession of single story, erosional-based, medium to fine-grained sandstones. This basal unit contains mud clasts, prominent trough cross-bedding, ripple cross-lamination, and coaly plant traces. It is overlain by thick-bedded, horizontally laminated, greyish claystones or silty claystones. These fine-grained deposits contain siderite concretions, abundant fragmented wood debris, and coaly traces (Fig. 3A). The succession grades upward into interbedded carbonaceous mudstones and coal deposits (Zhang, 2014; Fig. 2). These deposits are interpreted as distributary channel (basal sandstones), coastal floodbasin (claystones and silty claystones), and coastal mire (carbonaceous mudstones and coal) facies, respectively, collectively defining a delta plain facies association (Table 1). Critically, distinct tuffaceous mudstone horizons are intercalated within the coastal floodbasin deposits. These units are characterized by their white to pale grey colour, sharp upper and lower contacts, very fine-grained, homogenous appearance and absence of primary sedimentary structures (Fig. 3A). Their mineralogical composition, dominated by altered volcanic glass and clay minerals (Yang et al., 2020; Lu et al., 2021a), confirms an air-fall volcanic ash origin. The pristine preservation and lack of bioturbation or reworking within these tuffaceous layers indicate rapid deposition in low-energy, subaqueous conditions concomitant with the accumulation of ambient clay minerals. The overlying Lower Shihhotse Formation is characterized by 1–10 m thick succession of erosional based, coarse- to medium-grained sandstones. This sandstone succession displays trough cross-bedding, ripple cross-lamination, and mud clasts (Fig. 3B). Thin mudstone partings are locally intercalated in the lower portion. The upper part transitions into thick-bedded, mudstones with purple red mottling containing siderite concretions (Zhang, 2014; Figs. 2 and 3B). These deposits are interpreted as alluvial plain channel (sandstones) and floodplain (mudstones) deposits, respectively, forming an alluvial plain facies association (Table 1). Within the floodplain mudstones of the Lower Shihhotse Formation, discrete pale grey-colored tuffaceous mudstone beds occur (Fig. 3B). Similar to those in the Shansi Formation, these beds exhibit structureless, fine-grained fabric, consistent with discrete episodes of volcanic ash fall into the alluvial plain environment.

The fossil plant assemblages from the Shansi and Lower Shihhotse formations preserve evidence of a notable interval that experienced elevated levels of extinction within the Lower Shihhotse Formation (Stevens et al., 2011). This extinction event marks the disappearance of numerous taxa that initially emerged in the Taiyuan and Shansi formations, which in this region were represented by deposits of marginal marine and peatland settings (Stevens et al., 2011; Fig. 2).

3. Methods

Zircon U-Pb dating was conducted on two tuffaceous mudstone samples, one from the Shansi Formation (D11-7-TM1) and the other

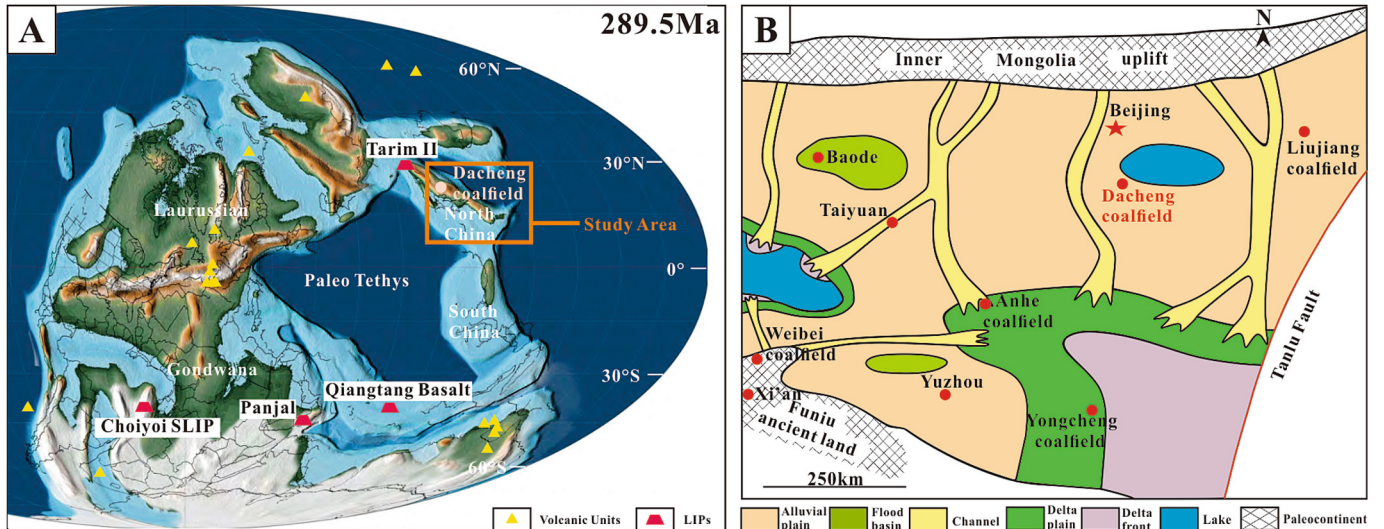


Fig. 1. (A) Global paleogeography at ~289.5 Ma (Scotese, 2014) emphasizing the location of the Dacheng coalfield, North China and the global igneous centers of the Tarim II, Panjal, Qiangtang Basalt, and Choiyoi silicic Large Igneous Provinces. The positions of other reported volcanic units dated at ~290–291 Ma are labeled based on Soreghan et al. (2019) and references therein. The suturing of the northern Laurussian and southern Gondwanan continents exemplifies the tectonic processes that led to the assembly of the supercontinent Pangea. (B) Paleogeographic map of North China during the deposition of Lower Shihhotse Formation, illustrating the locations of the Dacheng, Liujiang, Yongcheng, Baode, Anhe and Weibei coalfields (modified from Shao et al., 2014).

from the Lower Shihhotse Formation (D11-7-TM2) (Figs. 2, 3, and 4). After the samples underwent crushing, grinding, sieving, and separation through heavy liquid and magnetic separation methods, euhedral zircon crystals with clearly defined oscillatory zoning were identified using cathodoluminescence (CL) microscopy. These crystals were selected for U-Pb isotope analysis of zircon. Subsequently, the U, Th, and Pb isotopes within the zircon grains were analyzed by Laser Ablation Inductively Coupled Plasma Mass Spectrometry (LA-ICP-MS) at the Beijing Research Institute of Uranium Geology. DataCal and Isoplot 3.0 software were utilized for the age analysis, calculations, and for generating concordia diagrams based on the LA-ICP-MS data.

A total of 38 mudstone samples were collected from the Shansi and Lower Shihhotse formations from core D11-7 in the Dacheng coalfield, North China, including 20 samples in the Shansi Formation and 18 samples in the Lower Shihhotse Formation (Fig. 2). The vertical sampling locations are illustrated in Fig. 2. The mudstone samples were crushed to finer than 200 mesh (74 µm) and subsequently employed for comprehensive analyses, including determination of major elements (including Al, Ti, P) and trace elements (including Ni, Co, V, Mo targeted for volcanic and environmental proxies, and Sr and Ba targeted for paleosalinity), total organic carbon (TOC) and mercury (Hg) concentrations, and the carbon isotopic composition of bulk organic matter ($\delta^{13}\text{C}_{\text{org}}$). Analyses of major and trace elements, TOC and Hg concentrations, and $\delta^{13}\text{C}_{\text{org}}$ were conducted at the Beijing Research Institute of Uranium Geology.

For the analysis of major element content, sample powders were combined with dry lithium tetraborate and borax and then fused to form glass beads. The analytical procedure was carried out using an Axios X-ray fluorescence spectrometer (XRF), with a relative analysis error of $\pm 5\%$. For the analysis of trace element content, the sample powders were fused with lithium borate and subsequently dissolved in ultrapure nitric acid (HNO_3). The analytical performance was conducted using an ELEMENT XR inductively coupled plasma mass spectrometer (ICP-MS), achieving a relative analysis error of less than $\pm 5\%$.

Samples undergoing Hg concentration analysis were initially digested by heating in an aqua regia solution (composed of a 1:1 mixture of hydrochloric acid and nitric acid). Subsequently, the digested samples were subjected to reduction with a potassium borohydride (KBH_4) solution to its atomic form. The Hg concentration analysis was subsequently performed using an atomic fluorescence spectrometer (LC-

6500), which is equipped with a lower detection limit of 2 ng/g and a relative analysis error of $\pm 5\%$.

Samples for TOC and $\delta^{13}\text{C}_{\text{org}}$ analyses were initially treated with diluted phosphoric acid to eliminate inorganic carbon. The TOC concentrations were determined using a LECO carbon-sulfur analyzer (CS-580 A), which has a lower detection limit of 100 mg/g and an absolute analysis error of $\pm 0.2\%$. The $\delta^{13}\text{C}_{\text{org}}$ analyses were conducted using a Thermo Scientific 253 isotope ratio mass spectrometer. The $\delta^{13}\text{C}_{\text{org}}$ values are reported in per mil (‰) relative to the Vienna Pee Dee Belemnite (VPDB) standard, with an absolute analysis error of $\pm 0.1\%$.

To isolate the $\delta^{13}\text{C}_{\text{org}}$ signal from confounding influences, several independent proxies were employed: P/Ti ratio is used as a proxy for primary productivity, with higher values indicating increasing productivity (Dean et al., 1997; Algeo et al., 2011). Sr/Ba ratio is used as an indicator for paleosalinity, reflecting eustatic control ($\text{Sr/Ba} < 0.2$, 0.2–0.5, and > 0.5 indicating freshwater, brackish, and marine conditions, respectively, Wei and Algeo, 2020). Organic Carbon Accumulation Rate (OCAR) is used for indicating the organic carbon burial, calculated from TOC, a constant mudrock density of 2.5 g/cm^3 (Lv et al., 2025), and a linear sedimentation rate of $\sim 19.5 \text{ m/Myr}$ (validated by stable Al_2O_3 content). Separately, the $\text{V}/(\text{V} + \text{Ni})$ ratio is used to characterize the depositional redox conditions, with values < 0.6 , 0.6–0.84, and > 0.84 indicating oxic to suboxic, anoxic to sub-euxinic, and euxinic conditions, respectively (Hatch and Leventhal, 1992; Tribouillard et al., 2006; Qiao et al., 2016).

4. Results

4.1. Zircon U-Pb dating

The zircon grains within the tuffaceous mudstone layers exhibit a range of particle sizes, spanning from 50 to 150 µm (Fig. 5A). Individual zircon crystals exhibit well-defined euhedral shapes and distinct oscillatory zoning when observed under cathodoluminescence (CL) imaging, indicative of a first-cycle magmatic origin for these zircon grains (Fig. 5A). The Th/U ratios of the analyzed zircon grains range from 0.43 to 1.88 (Supplementary Table 1), which is consistent with the ratios typically observed in magmatic zircons (Zhu et al., 2013).

From sample D11-7-TM1, a total of 25 concordant age data points were obtained. The U-Pb isotope analyses of 17 zircon grains revealed a

Table 1

Summary of the description and interpretation of the facies associations and facies for the Shansi and Lower Shihhotse formations in the Dacheng coalfield, Hebei Province, North China.

Facies association/ Facies	Interpretation	Lithology	Sedimentary structures/ Fossils	Stratigraphic distribution
A 1	Alluvial plain Alluvial plain channel	1–10 m thick succession of erosionally based coarse- to medium- grained sandstone with mud clasts interbedded with thin partings of mudstone	Trough cross- bedding and ripple cross- lamination	Lower Shihhotse Formation
2	Floodplain	6–70 m thick succession of mudstone with purple/red mottling interbedded with thin sandstone partings	Ripple cross- lamination, horizontal lamination, siderite concretions	Lower Shihhotse Formation
B 3	Delta plain Distributary channel	1–8 m thick fining-upward succession of single story, erosionally- based medium- to fine-grained sandstone with mud clasts	Trough cross- bedding, ripple cross- lamination, coaly traces	Shansi Formation
4	Coastal floodbasin	Thick-bedded greyish claystone interbedded with thin bedded fine- grained sandstone	Ripple cross- lamination, horizontal lamination, siderite concretions, fragmented wood debris, and coaly traces	Shansi Formation
5	Coastal mire	1–5 m thick coal and carbonaceous mudstone		Shansi Formation

concordance greater than 90 %, exhibiting near-concordant $^{206}\text{Pb}/^{238}\text{U}$ ages that span from 276 ± 3 Ma to 299 ± 5 Ma. The calculated weighted mean age of these zircon grains is 290.7 ± 3.3 Ma (Fig. 5B and C; Supplementary Table 1). Sample D11-7-TM2 produced 22 concordant age determinations, with the U-Pb isotope analyses of 21 zircon grains exhibiting a concordance exceeding 90 %. 17 zircon grains exhibit younger near-concordant $^{206}\text{Pb}/^{238}\text{U}$ ages, ranging from 279 ± 4 Ma to 296 ± 4 Ma. The weighted mean age of these grains is 289.4 ± 1.8 Ma (Fig. 5D and E; Supplementary Table 1). Four additional zircon grains exhibit older, near-concordant $^{206}\text{Pb}/^{238}\text{U}$ ages, which vary from 311 ± 4 Ma to 362 ± 4 Ma (Supplementary Table 1).

The mean zircon ages of the main cluster from tuffaceous mudstone deposits correspond to Sakmarian to Artinskian ages. Consequently, the weighted mean ages derived from younger peaks were interpreted to represent the depositional ages of these tuffaceous mudstones. Critically, these depositional ages are anchored by a pivotal high-precision CA-ID-TIMS U-Pb age of 295.65 ± 0.11 Ma (Yang et al., 2020),

obtained from tuffaceous mudstone beneath the topmost limestone near the Taiyuan-Shansi formation boundary in the Yongcheng coalfield. This age, biostratigraphically constrained within the *Streptognathodus fusus* conodont zone and correlative with topset limestones in the Dacheng coalfield (Shen et al., 2019; Fig. 2), provides an absolute chronological framework. Within this framework, integration of two newly obtained LA-ICP-MS zircon ages (samples D11-7-TM1 and D11-7-TM2) enabled application of an average sedimentation rate of $\sim 19.5 \pm 5.6$ m/Myr to the Dacheng coalfield and constrained the Shansi-Lower Shihhotse Formation boundary to ~ 289.8 Ma (Figs. 2 and 4). This boundary age aligns with the ~ 290 Ma boundary reported for equivalent positions by Yang et al. (2014, 2016, 2020); (Fig. 4) and corresponds to the Sakmarian-Artinskian stage boundary.

Sedimentation rates for the Shansi Formation, derived from CA-ID-TIMS U-Pb dating and age models, are 16.9 m/Myr in the Yongcheng coalfield (Yang et al., 2020) and 22.1 ± 0.2 m/Myr in the Baode section (Wu et al., 2021). Given the relatively uniform sedimentary characteristics across North China, the Dacheng coalfield exhibits sedimentation rates consistent with these published rates. Using the anchored 295.6 ± 0.1 Ma (CA-ID-TIMS) age at the Taiyuan-Shansi Formation boundary and applying the ~ 19.5 m/Myr sedimentation rate, linear interpolation (without applying differential compaction correction or considering different deposition rates in the Dacheng coalfield) delineates the Shansi and Lower Shihhotse formations within the 295.6 and 284.2 Ma interval (Supplementary Table 2; Fig. 2). The uncertainty at 284.2 Ma (± 2.4 Ma) reflects the propagation of the sedimentation rate error (± 5.6 m/Myr) over the relevant depth interval.

Furthermore, the constructed age model for the Dacheng coalfield aligns with other reported CA-ID-TIMS U-Pb dating results from the Baode section and LA-ICP-MS U-Pb dating results from the Lijiang coalfield (Yang et al., 2020; Wu et al., 2021; Fig. 4). This includes the ages of the Shansi Formation of 295.962 ± 0.086 Ma and 295.346 ± 0.080 Ma in the Baode section (Wu et al., 2021; Fig. 4), and the age of the lower Shansi Formation of 290.1 ± 3.0 Ma (Wang et al., 2023; Fig. 4). However, the overall age of the Lower Shihhotse Formation in the Baode section (Wu et al., 2021) appears older than that observed in the Yongcheng, Dacheng, and Lijiang coalfields (Yang et al., 2020; Wang et al., 2023; Fig. 4), while the Shansi Formation age in the Lijiang coalfield (Wang et al., 2023) is younger than that observed in the Yongcheng, Dacheng, and Baode sections (Yang et al., 2020; Wu et al., 2021; Fig. 4). This discrepancy likely reflects diachronism of Permian lithostratigraphic units across North China, potentially influenced by considerable geographical distances between sites (Wang, 1997; Shen et al., 2022a).

4.2. Hg, Ni, and supplementary volcanic indicators (Co, V, Mo) concentrations

In the sampled stratigraphic section from the Dacheng coalfield, Hg concentrations exhibit considerable variability through the Shansi Formation, with elevated values overall, ranging from 24.8 to 201 ppb and averaging 58.1 ppb (Supplementary Table 2; Fig. 6). Three distinct Hg peaks exceeding 90 ppb are evident, corresponding to 293.0 Ma, 292.2 Ma, and 291.0 Ma, respectively (Fig. 6). In contrast, Hg concentrations through the Lower Shihhotse Formation are notably lower and less variable, ranging from 8 to 43.1 ppb, with an average of 26.1 ppb (Supplementary Table 2; Fig. 6).

From the Shansi Formation to the Lower Shihhotse Formation, the concentration of Ni fluctuates between 12.3 and 39.9 ppb, with an average concentration of 24.3 ppb (Supplementary Table 2; Fig. 6). In the sampled vertical section from the Dacheng coalfield, the Ni concentration does not display any pronounced Ni anomaly above the background level of roughly 24.3 ppb (Fig. 6).

Beyond serving as volcanic indicators, Co, V, Mo, and Ni exhibit

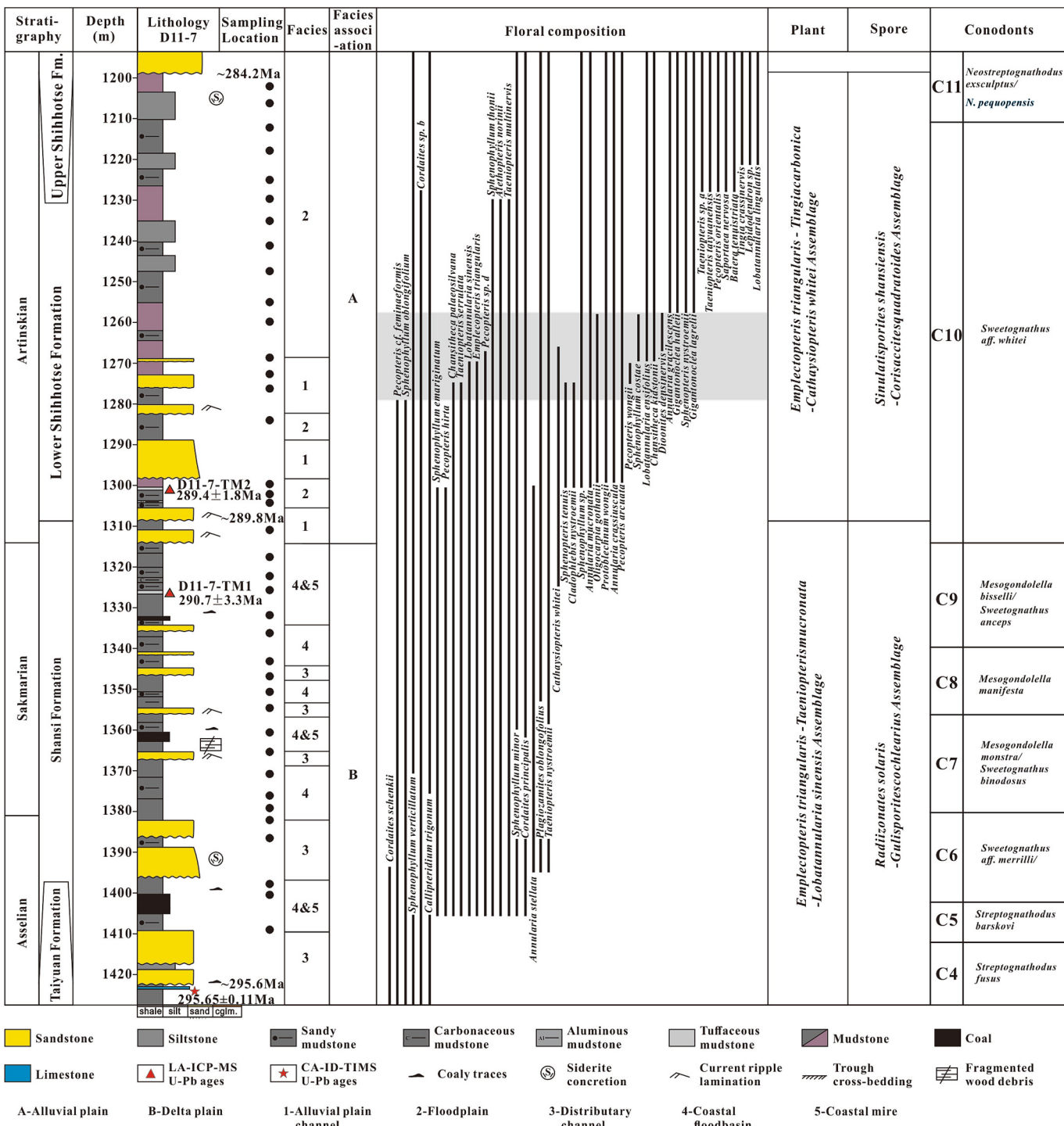


Fig. 2. Stratigraphic log of core hole D11-7 spanning from the Shansi Formation to the Lower Shihhotse Formation in the Dacheng coalfield, North China. The black dots denote mudstone samples. Codes for Facies and Facies associations are according to Table 1. Fossil plant species are referenced from the Eastern and Western Hills section in Taiyuan, Shanxi Province, as documented by Stevens et al. (2011). Macrofossil plant assemblages and spore assemblages are referenced from the Weibei coalfield, as reported by Wang (2010). The extinction episode marked in the Lower Shihhotse Formation (grey shading in Fig. 2) corresponds to a facies transition from peat-forming mire to fluvio-deltaic deposits (Stevens et al., 2011). During this extinction event, 14 of the 31 documented plant species disappear, signifying a 45 % extinction rate among the plant species (Stevens et al., 2011). The conodont zonation is cited from Shen et al. (2019). The age model is constrained by radiometric ages from tuffaceous mudstone samples (D11-7-TM1 and D11-7-TM2) within the Dacheng coalfield, and a CA-ID-TIMS age for the topmost Taiyuan Formation in the Yongcheng coalfield (Yang et al., 2020).

distinct redox sensitivities across an oxic to euxinic gradient (Tribovillard et al., 2006). Co could enrich under anoxic conditions via insoluble CoS formation (Huerta-Diaz and Morse, 1992). V accumulates from suboxic to anoxic environments, with maximal enrichment under euxinic conditions (Breit and Wanty, 1991; Algeo and Maynard, 2004).

Mo fixes primarily in persistently euxinic environments (Helz et al., 1996; Erickson and Helz, 2000), and Ni forms insoluble sulfides primarily under strong reducing conditions (Tribovillard et al., 2006). Concentration profiles across the Shansi to Lower Shihhotse Formation from the Dacheng coalfield show that Co remains relatively stable, with

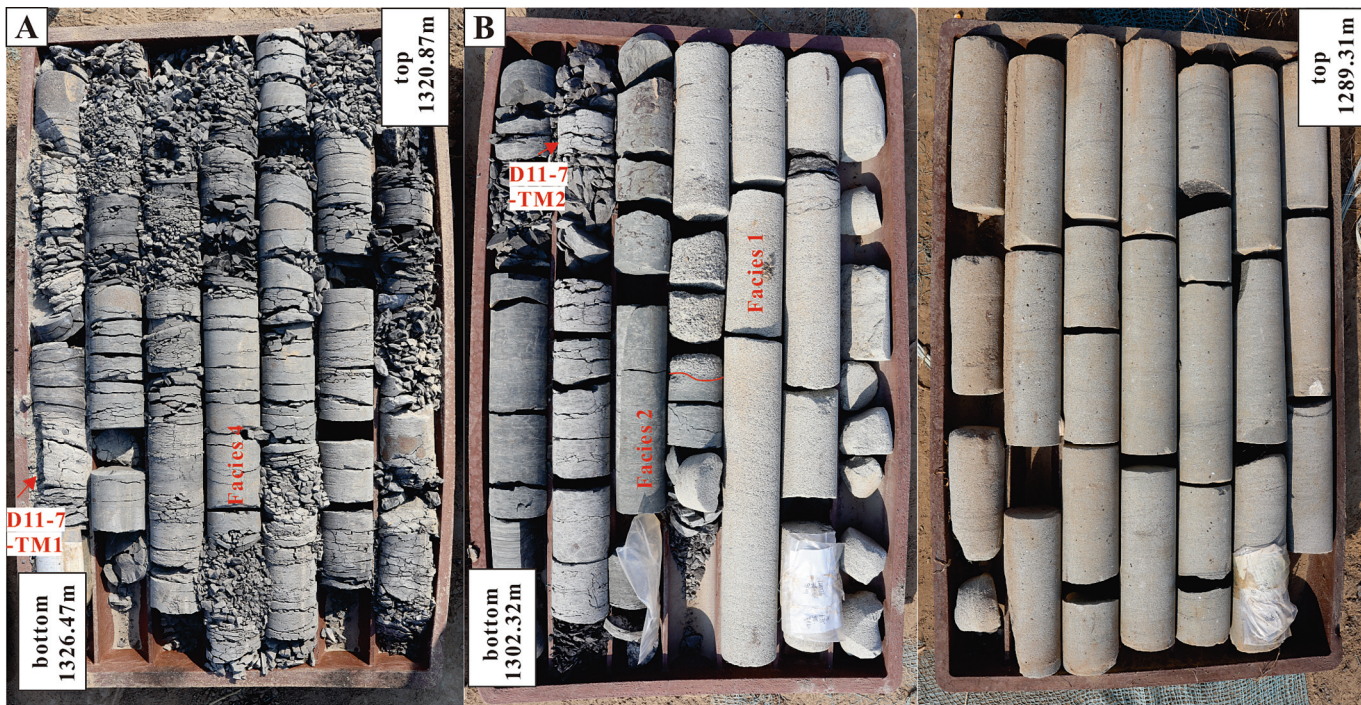


Fig. 3. Core photographs illustrating representative facies and key tuffaceous mudstone layers in the Shansi and Lower Shihhotse formations. (A) Horizontally laminated greyish to grey-black claystones (Facies 4: coastal floodbasin) intercalated with a distinctive white to pale grey tuffaceous mudstone layer (D11-7-TM1) with the sharp upper and lower contacts, homogeneous, structureless fabric, and absence of primary sedimentary structures, depths from 1326.47 to 1320.87 m, Shansi Formation. (B) Greyish claystones transitioning upward into purple-reddish mottled mudstones (Facies 2: floodplain), interrupted by a pale grey tuffaceous mudstone layer (D11-7-TM2) exhibiting a structureless texture. The mudstone succession is overlain by an erosional based, coarse- to medium-grained sandstone displaying trough cross-bedding (Facies 1: alluvial plain channel), depths from 1302.32 to 1289.31 m, Lower Shihhotse Formation. Codes for Facies are according to Table 1. (For interpretation of the references to colour in this figure legend, the reader is referred to the web version of this article.)

two exceptions at 291.6 Ma and 291.0 Ma (Fig. 6). V displays an overall decreasing trend without distinct anomalies, aligning with persistently sub-euxinic conditions ($V/(V + Ni)$ primarily 0.6–0.84) that inhibit reduction to particulate forms (Tribouillard et al., 2006; Fig. 6). Mo exhibits fluctuations, with relatively high concentrations over 2.4 $\mu\text{g/g}$ at 292.2 Ma and 291.0 Ma (Fig. 6).

4.3. TOC and Al_2O_3 values

The data for TOC and Al_2O_3 concentrations are presented in Supplementary Table 2 and illustrated in Fig. 6. The Shansi Formation is characterized by elevated TOC concentrations, ranging from 0.30 wt% to 4.26 wt%, and exhibiting an average of 1.42 wt% (Supplementary Table 2; Fig. 6). In contrast, the Lower Shihhotse Formation is characterized by lower TOC values, ranging from 0.06 wt% to 2.21 wt%, with an average of 0.56 wt% (Supplementary Table 2; Fig. 6).

The concentration of Al_2O_3 fluctuates between 10.8 % and 28.4 %, with an average concentration of 20.5 % (Supplementary Table 2). Al_2O_3 concentrations decrease from the Shansi Formation upward into the Lower Shihhotse Formation (Fig. 6).

To account for the effects of redox conditions and detrital input on Hg and Ni concentrations, the inter-relationships among these variables were examined. Hg concentrations exhibit a weak positive correlation with TOC, with a correlation coefficient (R^2) of 0.25 and P value <0.01 based on 38 samples. The correlation between Hg and Al is negligible, as indicated by an R^2 value of 0.13 and P value <0.01 based on 38 samples (Fig. 7A and B). The absence of a significant correlation between Hg and Al in coastal sediment deposits, despite the presence of substantial terrigenous material, can be ascribed to disparities in their origins and the mechanisms of their deposition. The Ni concentrations display no

significant correlation with either TOC ($R^2 = 0.0002$, $P < 0.01$, $n = 38$) or Al ($R^2 = 0.0021$, $P < 0.01$, $n = 38$). These results suggest that the nickel concentrations are likely influenced by external factors rather than being a consequence of the redox conditions and detrital input (Fig. 7C and D).

To account for the influence of redox conditions, Hg concentrations were normalized to TOC in this study. However, it is important to note that potential errors in the Hg/TOC may be amplified when the measured TOC levels approach the lower detection limits of the analytical methods employed. Any measurement error in the TOC values can also impact the Hg/TOC ratio. Consequently, Hg/TOC values should not be calculated for samples with less than 0.2 wt% TOC to avoid inaccuracies (Grasby et al., 2013, 2019). Here, we eliminated the samples with less than 0.4 wt% TOC from further examination (Supplementary Table 2 and Fig. 6). The Hg/TOC ratios range from 9.2 to 106.1 ppb/wt%, with an average ratio of 40.0 ppb/wt% (Supplementary Table 2). The Hg/TOC ratios exhibit one distinct peak at a level corresponding to 291.0 Ma, which correlates strongly with one of the Hg anomalies (Fig. 6).

4.4. $\delta^{13}\text{C}_{\text{org}}$ values

The carbon isotopic composition of organic matter ($\delta^{13}\text{C}_{\text{org}}$) ranges from -28.6 to -23.3 ‰, with an average of -25.5 ‰ (Supplementary Table 2). The $\delta^{13}\text{C}$ values reported for ancient C3 plants typically fall within the range of -23 to -27 ‰, with an average of -24 ‰ (Gröcke, 2002). In contrast, marine organic matter usually exhibits a $\delta^{13}\text{C}$ value of -22 ‰ (Meyers, 1997). From the Shansi Formation to the Lower Shihhotse Formation, there is an overall long-term trend towards lower values, with the variation exceeding 5 %. Within the Shansi Formation,

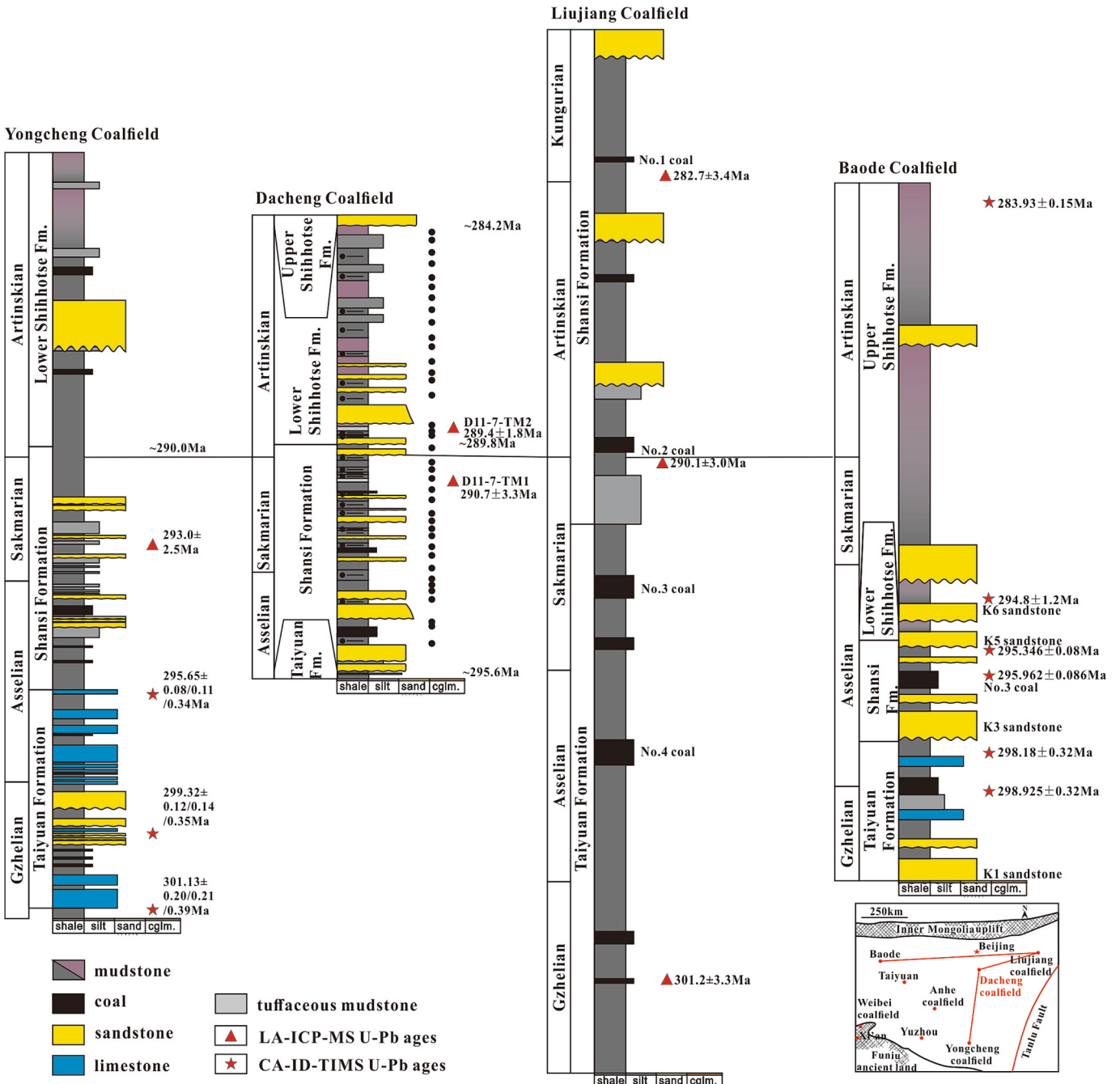


Fig. 4. Chronostratigraphic and lithostratigraphic correlation of Sakmarian to Artinskian in the North China Basin. The black dots denote the mudstone samples used for elemental composition, TOC, Hg, and $\delta^{13}\text{C}_{\text{org}}$ analyses. Lithology and age data of the sections at Yongcheng (Yang et al., 2014; Yang et al., 2020), Dacheng (this study), Liujiang (Wang et al., 2023), and Baode (Wu et al., 2021) are organized from south to north and from east to west. These section locations are marked in the lower-right panel.

four negative isotope excursions are identified, with variations of 2.1 ‰, 1.8 ‰, 1.8 ‰, and 2.3 ‰, which all occurred during the Sakmarian stage. These excursions correspond to several spikes in Hg and Hg/TOC ratios (Fig. 6). In the Lower Shihhotse Formation, three negative isotope excursions are noted within the Artinskian stage, with variations of 4.1 ‰, 3.3 ‰, and 1.7 ‰ (Fig. 5). The concentration of Al_2O_3 exhibits a cyclical trend, characterized by an overall decline that mirrors the pattern observed in the $\delta^{13}\text{C}_{\text{org}}$ values (Fig. 6). However, the negative excursions in $\delta^{13}\text{C}_{\text{org}}$ do not align well with the intervals of low Al_2O_3 concentration, and the fluctuations in the Al_2O_3 record do not show a strong correlation with the lithological changes in the Shansi and Lower

Shihhotse formations (Fig. 6). As a result, the variations in $\delta^{13}\text{C}_{\text{org}}$ do not appear to be associated with lithofacies. It is more likely that the changes in $\delta^{13}\text{C}_{\text{org}}$ values and Al_2O_3 concentrations are influenced by other controlling factors.

5. Discussion

5.1. Carbon isotope correlation

Carbon stable isotope profiles are widely recognized as a fundamental proxy for tracking changes in the global carbon cycle and have been used

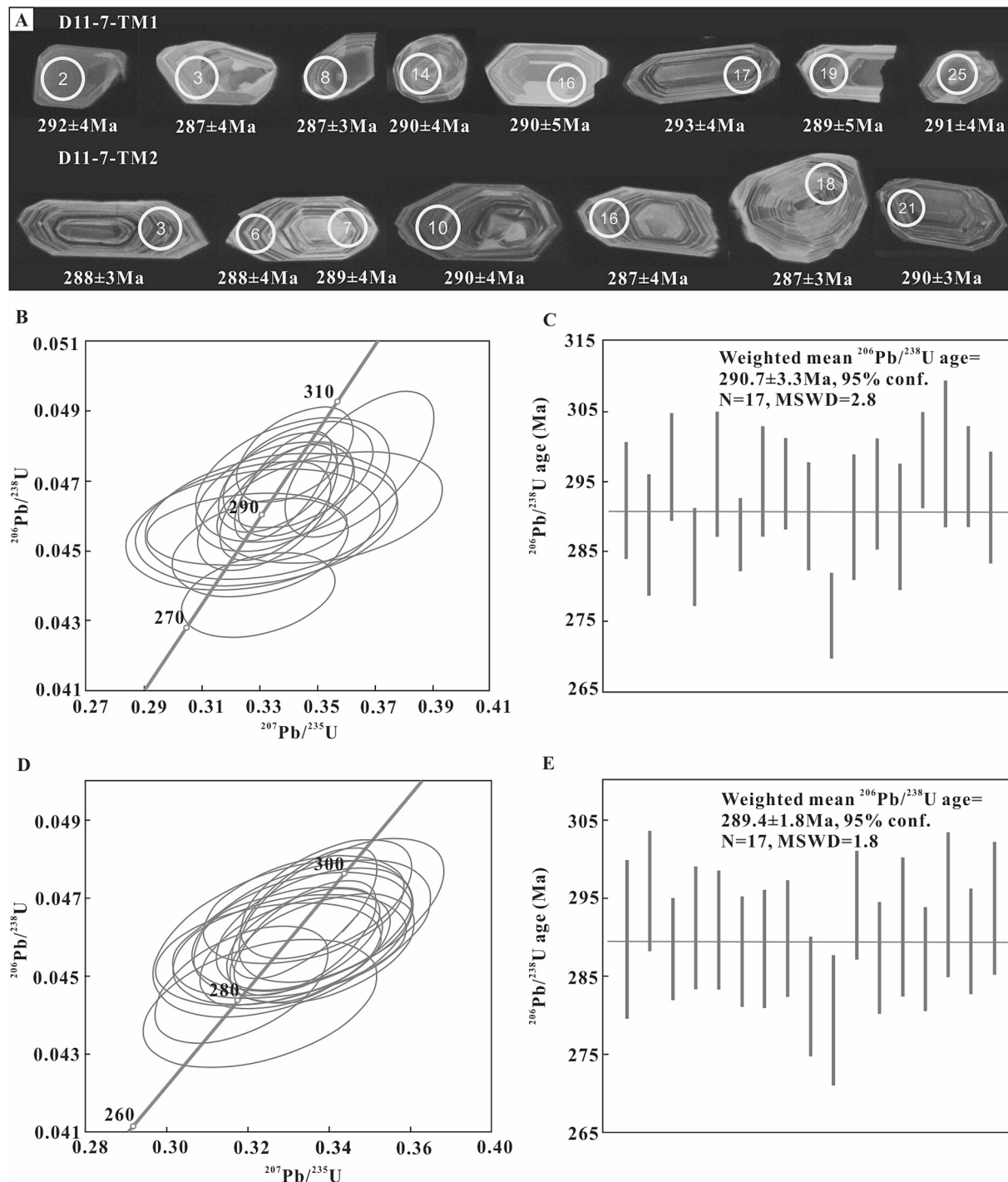


Fig. 5. (A) Cathodoluminescence (CL) images showing the internal structures of zircons from the tuffaceous mudstone samples D11-7-TM1 and D11-7-TM2. The white circles, accompanied by numerical labels, denote the laser ablation spots used for LA-ICP-MS U-Pb dating. (B) Zircon U-Pb concordia plot and (C) weighted mean $^{206}\text{Pb}/^{238}\text{U}$ age of tuffaceous mudstone sample D11-7-TM1. Abbreviations: MSWD = mean square of weighted deviations. (D) Zircon U-Pb concordia plot and (E) weighted mean age of tuffaceous mudstone sample D11-7-TM2. Abbreviations: MSWD = mean square of weighted deviations.

extensively in chemostratigraphic correlations (Ishikawa et al., 2008; Le Guerroué and Cozzi, 2010; Tang et al., 2011; Zeng et al., 2012; Lu et al., 2021b; Sun et al., 2022b). The Cisuralian $\delta^{13}\text{C}$ records presented here are derived from a range of geographically dispersed marine and terrestrial successions (Zhang et al., 1999; Korte et al., 2005; Montañez et al., 2007; Frank et al., 2008, 2015; Birgenheier et al., 2010; Tierney, 2010; Koch and Frank, 2012; Zeng et al., 2012; Liu et al., 2017; Lu et al., 2021b; Sun et al., 2022b; Fielding et al., 2023; Wang et al., 2023). The isotopic shifts in these records are influenced by a range of local to global factors, including

the source of carbon (marine vs terrestrial), regional environmental fluctuations, and fluxes between global carbon reservoirs (Meyers, 1997; Hayes et al., 1999; Gröcke, 2002). To minimize local influences, the datasets were synthesized and plotted within a unified temporal framework to allow interpretation of global patterns. This was achieved by utilizing absolute age determinations (reported CA-ID-TIMS age from Yang et al., 2020 and dated tuffaceous mudstones D11-7-TM1 and D11-7-TM2) and biostratigraphic correlation data (conodont zonation of Shen et al., 2019), while also incorporating the latest adjustments to the

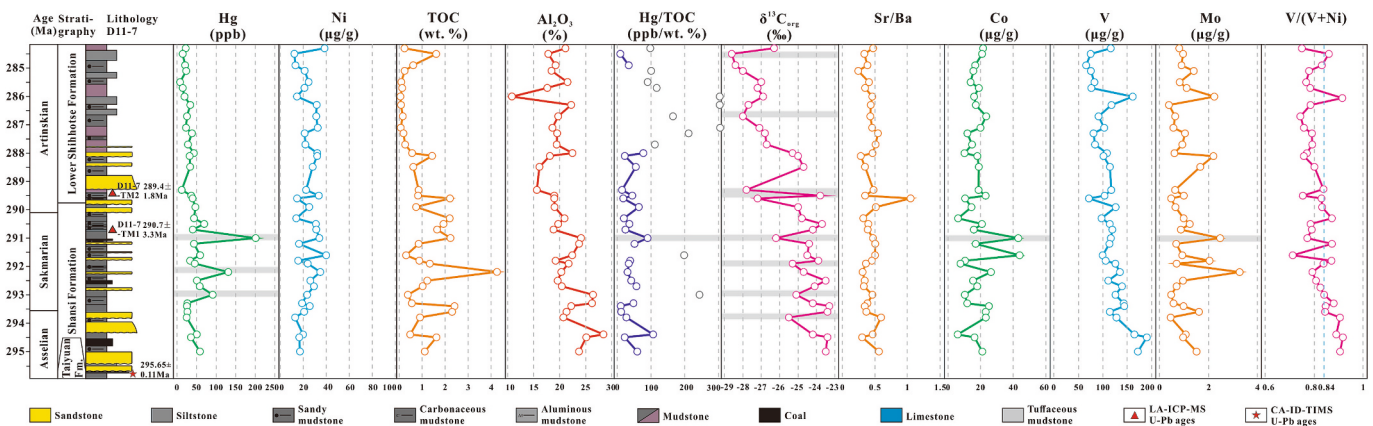


Fig. 6. The vertical profiles illustrate variations in geochemical parameters, including Hg and Ni concentrations, TOC values, Al_2O_3 concentrations, Hg/TOC ratios, $\delta^{13}\text{C}_{\text{org}}$ values, Sr/Ba ratio, Co, V, Mo concentrations, and V/(V + Ni) ratios in the Dacheng coalfield over the time span from 295.6 Ma to 284.2 Ma. Notably, the grey dots on the Hg/TOC curves represent Hg/TOC ratios that were not calculated for samples containing less than 0.4 wt% TOC. The grey bars in the diagram highlight intervals exhibiting the elevated Hg concentrations and Hg/TOC ratios, negative excursions in the $\delta^{13}\text{C}_{\text{org}}$ values, peaks in Co and Mo concentrations at ~291 Ma. The Sr/Ba ratios consistently suggest brackish conditions (Wei and Algeo, 2020), except for one anomaly (1.05 at 289.6 Ma). V/(V + Ni) ratios predominantly in the range of 0.6 to 0.84 reflect sub-euxinic conditions (Hatch and Leventhal, 1992; Tribouillard et al., 2006; Qiao et al., 2016). The stratigraphic variations are detailed in Fig. 2. The age model is constrained by radiometric ages from tuffaceous mudstone samples (D11-7-TM1 and D11-7-TM2) within the Dacheng coalfield, and a CA-ID-TIMS age marking the top of the Taiyuan Formation in the Yongcheng coalfield (Yang et al., 2020).

Permian geological time scale (<http://www.stratigraphy.org/ICSchart/ChronostratChart2024-12>; Fig. 8). Multi-proxy evaluation rules out significant influences from primary productivity (no covariation with P/Ti ratios; Fig. 7E), vegetation type (persistent C3 dominance confirmed by macrofossil plant assemblages of Wang, 2010), kerogen and maceral compositions dominated by Type III and vitrinite and inertinite, respectively, reported by Zhang et al., 2025), organic carbon burial (negligible correlation with organic carbon accumulation rate; Fig. 7F and Supplementary Table 2), microbial activity and methane release (implausible under subeuxinic brackish conditions; Fig. 6), or eustasy (stable Sr/Ba ratios predominantly in the range of 0.2–0.5 indicating brackish water conditions; Fig. 6) on the $\delta^{13}\text{C}_{\text{org}}$ signal in the North China section.

During the Asselian to early-middle Sakmarian, $\delta^{13}\text{C}_{\text{org}}$ values in the Dacheng coalfield of North China show a pattern of recurrent fluctuations (Fig. 8). This pattern corresponds to the period characterized by a relatively long-term positive trend of $\delta^{13}\text{C}_{\text{org}}$ data from the Midland Basin in Texas, USA (Montañez et al., 2007) and eastern Australia (Birgenheier et al., 2010; Fielding et al., 2023), as well as the $\delta^{13}\text{C}_{\text{carb}}$ records from the Gongchuan Section, South China (Liu et al., 2017), the Orogena Basin, New Mexico, USA (Koch and Frank, 2012), the Rockland Section in Nevada, USA (Tierney, 2010), and the Southern Ural region of Russia (Zeng et al., 2012; Fig. 8). This interval corresponds to the timing of the P1 glaciation event (Fielding et al., 2023) and likely records a complex climatic regime superimposed by numerous shorter glacial-interglacial cycles throughout the P1 Glacial period.

The $\delta^{13}\text{C}_{\text{org}}$ values in the Dacheng coalfield of North China exhibit an overall decreasing trend across the Sakmarian to Artinskian transition, despite some fluctuations (Fig. 8). This negative excursion is also evident in the $\delta^{13}\text{C}_{\text{org}}$ profiles from eastern Australia (Birgenheier et al., 2010; Fielding et al., 2023) and the $\delta^{13}\text{C}_{\text{carb}}$ records from the Gongchuan Section in South China (Liu et al., 2017), the Orogena Basin in New Mexico, USA (Koch and Frank, 2012), and the Southern Ural region of Russia (Zeng et al., 2012; Fig. 8). Additionally, $\delta^{13}\text{C}_{\text{org}}$ data from the Midland Basin in Texas, USA (Montañez et al., 2007) and $\delta^{13}\text{C}_{\text{carb}}$ data from the Rockland Section in Nevada, USA (Tierney, 2010) show a long-term negative trend starting from the late Sakmarian (Fig. 8). Although terrestrial $\delta^{13}\text{C}_{\text{org}}$ signals typically exhibit weaker global synchronicity than marine counterparts due to localized carbon pool influences, correction for regional biases reveals predominant directional depletion across most sections during this climatic transition. Significant amplitude variations persist (e.g. -4 ‰ to -12 ‰ shifts in the Rockland

Section and Southern Ural versus ~ -2 ‰ trend in other sections; Fig. 8), while some sections exhibit minimal isotopic response. Crucially, this directional alignment chronologically corresponds with the documented global negative $\delta^{13}\text{C}$ excursion limb (Liu et al., 2017) that coincides with reconstructed atmospheric $p\text{CO}_2$ increases (Montañez et al., 2007; Richey et al., 2020). Given that CO_2 is a potent greenhouse gas, the overall decline in $\delta^{13}\text{C}$ values record the addition of ^{13}C -depleted carbon to the atmosphere, indicative of climate warming (Isozaki et al., 2007a, 2007b; Frank et al., 2015). This timing is generally consistent with the deterioration of the P1 glaciation in both eastern and western Australia, the Paraná region in Brazil, western Argentina, Antarctica, Saudi Arabia, and Siberia during the Sakmarian-Artinskian transition (Domack et al., 1993; Chumakov, 1994; Isbell et al., 2003; Montañez and Poulsen, 2013; Fielding et al., 2008, 2023; Frank et al., 2015). This correspondence validates the climatic significance of the locally-corrected $\delta^{13}\text{C}$ signal.

5.2. Possible influences on Hg anomalies

Previous compilations have shown that Hg concentrations in sedimentary rocks typically range from 30 to 50 µg/kg (Grasby et al., 2019). More recent research, however, indicates that the average Hg concentration in sedimentary rocks, predominantly shales, is higher at 62.4 µg/kg, according to Grasby et al. (2019). Elevations in Hg concentrations above the local background levels tend to be indicative of volcanic activity or other outliers.

Documented, large-scale Sakmarian-Artinskian volcanic activity, as reported in the published literature, includes Tarim II LIP, Panjal Traps LIP, Qiangtang Basalt, and Choiyoi SLIP (Fig. 9). Episode II of the Tarim Large Igneous Province (LIP) was characterized by the eruption of widespread basalts, rhyolites, and pyroclastics (Xu et al., 2014) between 292 and 287 Ma, with the peak of volcanic activity at ~290 Ma (Xu et al., 2014; Fig. 9). The volcanic episode of the Panjal Traps LIP is predominantly marked by an extensive coverage of basalts, along with minor felsic rocks, dated to approximately ~289 ± 3 Ma (Shellnutt et al., 2011; Fig. 9). The Qiangtang Basalt dominated by mafic dykes is estimated at ~287 Ma (Zhang and Zhang, 2017; Fig. 9), and the Choiyoi SLIP started at ~286.5 ± 2.3 Ma (Sato et al., 2015; Fig. 9). Additional reported volcanic units dated at ~290–291 Ma are plotted in Fig. 1A (Soreghan et al., 2019). As the geographically closest volcanic units to the study area, the peak age of the Tarim II LIP coincides with the late

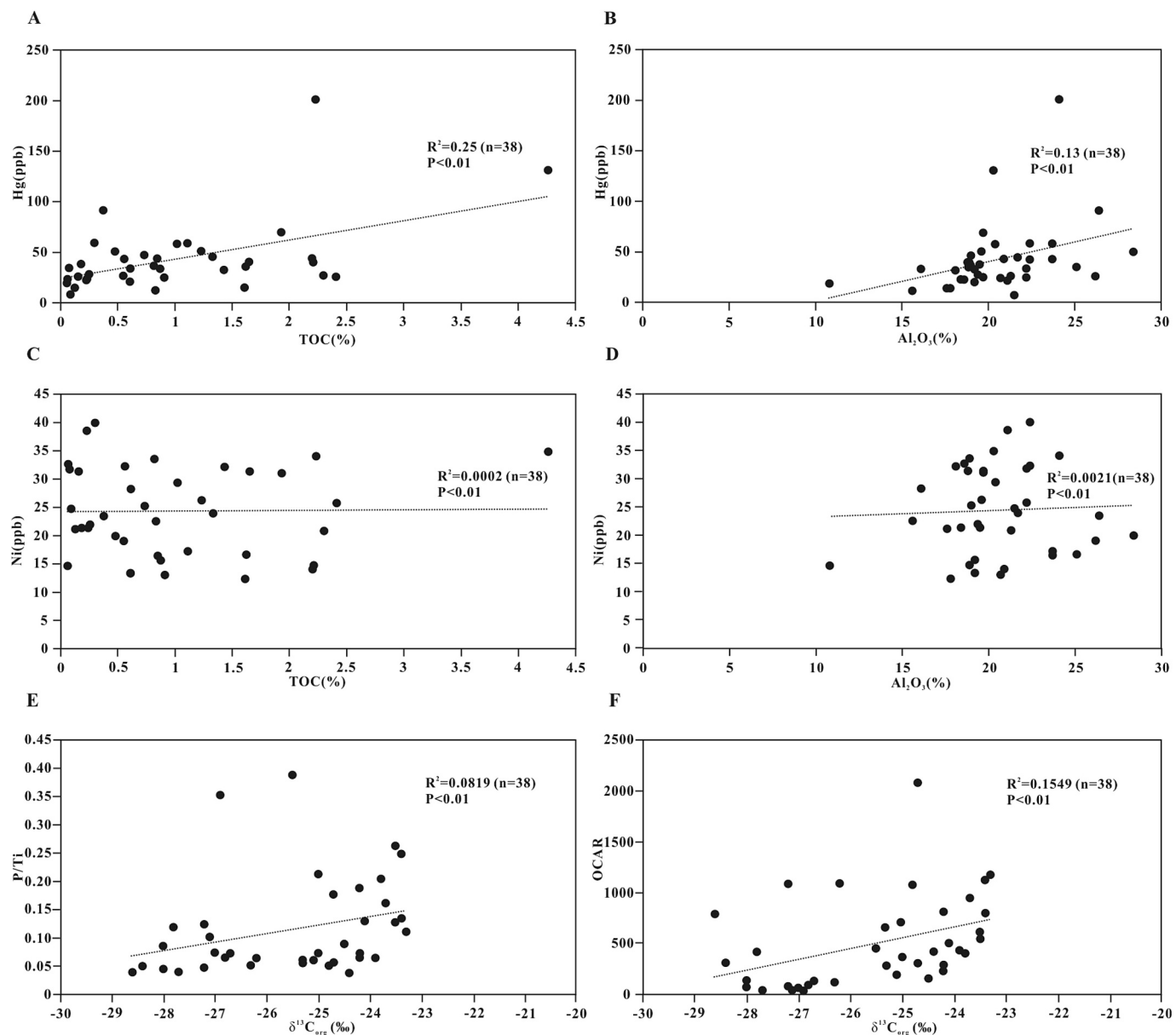


Fig. 7. Cross-plots of mercury (Hg) versus (A) total organic carbon (TOC) and (B) aluminum oxide (Al_2O_3), nickel (Ni) versus (C) total organic carbon (TOC) and (D) aluminum oxide (Al_2O_3), and $\delta^{13}\text{C}_{\text{org}}$ versus (E) P/Ti ratios and (F) Organic carbon accumulation rate (OCAR). The correlation coefficient (R^2), P value and the number of samples (n) are provided for each plot.

Sakmarian Hg and Hg/TOC anomalies (Fig. 9). This correlation is further corroborated by consistent findings from the Yuzhou section (Lu et al., 2021b; Fig. 9). In contrast, the reported ages of other potential volcanic sources, which are more distant geographically, are all younger than this event. The absence of coeval proximal volcanism reinforces the Tarim II LIP as the most viable driver for the 291 Ma event in the study area. Moreover, Artinskian Hg and Hg/TOC anomalies in the Liujiang and Yuzhou coalfields appear to correlate well with the timing of the Qiangtang Basalt (Lu et al., 2021b; Wang et al., 2023; Fig. 9), but the global multi-proxy environmental change may have started before the main eruption phase of the Qiangtang Basalt, and more likely started at the late Sakmarian (Figs. 8 and 9).

Extrusive and intrusive volcanic activities release substantial quantities of CO_2 that is relatively enriched in ^{13}C (with $\delta^{13}\text{C}$ values ranging from $-5\text{\textperthousand}$ to $-8\text{\textperthousand}$, as reported by Javoy et al., 1986) as well as Hg, leading to enrichment of Hg and an increase in atmospheric $p\text{CO}_2$

(Grasby et al., 2019; Vervoort et al., 2019). However, the intrusion of magma into organic matter-rich deposits could release substantial quantities of ^{13}C -depleted CO_2 (with $\delta^{13}\text{C}$ values around $-22\text{\textperthousand}$, or even more negative $\delta^{13}\text{C}$ values typically associated with terrigenous sources, e.g., peat or coal) and CH_4 (with $\delta^{13}\text{C}$ values around $-60\text{\textperthousand}$) into the atmosphere (Kump and Arthur, 1999; Svensen et al., 2004, 2009; Heydari et al., 2008). This intrusive process leads to an increase in atmospheric $p\text{CO}_2$, a decrease in $\delta^{13}\text{C}$ values of the contemporary atmosphere (McElwain et al., 2005), and a negative excursion in $\delta^{13}\text{C}_{\text{org}}$ values recorded in contemporary strata. It is evident that the Tarim LIP intruded into Paleozoic organic-rich rocks within the Tarim Basin, which triggered the maturation of source rocks and the activation of hydrocarbon fluids, leading to explosive release of methane through volcanic vents (Zhu and Zhang, 2022). It has been estimated that roughly 7062.5 gigatons (Gt) of methane ($\delta^{13}\text{C} = -60\text{\textperthousand}$) were released from the sedimentary succession of the Tarim Basin during the eruption

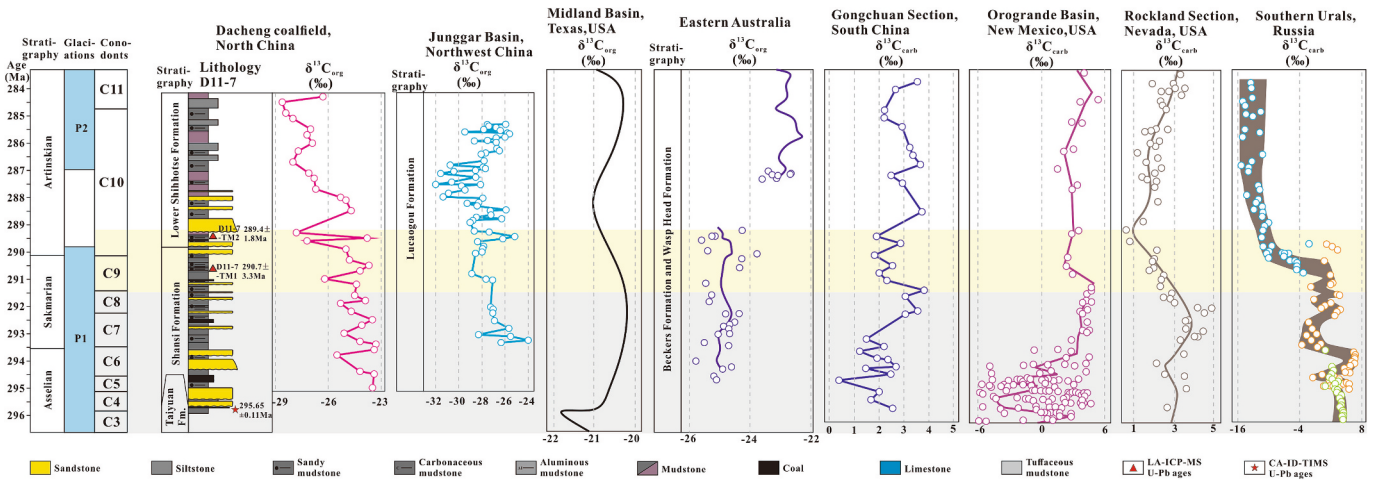


Fig. 8. Compilations of $\delta^{13}\text{C}_{\text{org}}$ data from the Dacheng coalfield (this study), the Junggar Basin of Northwest China (Sun et al., 2022b), the Midland Basin, Texas, USA (Montañez et al., 2007), and eastern Australia (Birgenheier et al., 2010; Fielding et al., 2023), along with $\delta^{13}\text{C}_{\text{carb}}$ datasets from the Gongchuan Section, South China (Liu et al., 2017), the Orogrande Basin, New Mexico, USA (Koch and Frank, 2012), the Rockland Section, Nevada, USA (Tierney, 2010), and the Southern Urals, Russia (Zeng et al., 2012). The data were screened for diagenetic effects and plotted on the absolute timescale. The temporal framework for glaciations in eastern Australia is based on the work of Fielding et al. (2023). The conodont zonation follows Shen et al. (2019), with detailed biozones presented in Fig. 2. The C3 zone is defined by the index fossil *Streptognathodus constrictus*. The stratigraphic variations are detailed in Fig. 2. The age model is constrained by radiometric ages from tuffaceous mudstone samples (D11-7-TM1 and D11-7-TM2) within the Dacheng coalfield, and a CA-ID-TIMS age marking the top of the Taiyuan Formation in the Yongcheng coalfield (Yang et al., 2020). Numerical timescale after <http://www.stratigraphy.org/ICSchart/ChronostratChart2024-12>. The greyish block delineates the temporal span from the Asselian to early-middle Sakmarian, while the yellow block signifies the interval encompassing the Sakmarian to Artinskian transition. (For interpretation of the references to colour in this figure legend, the reader is referred to the web version of this article.)

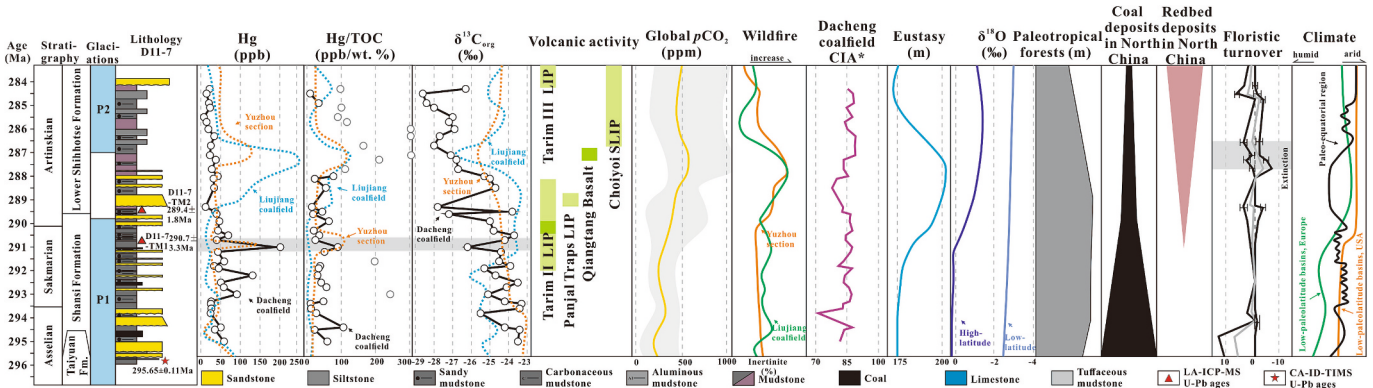


Fig. 9. Compilations of global events during the Sakmarian to Artinskian stages. The concentrations of Hg, the Hg/TOC ratios, and $\delta^{13}\text{C}_{\text{org}}$ data in the Dacheng coalfield are juxtaposed with the corresponding data from the Yuzhou section and Liujiang coalfield for comparative analysis (Lu et al., 2021b; Wang et al., 2023). The volcanic activity associated with the Tarim II LIP, Panjal Traps LIP, Qiangtang Basalt and Choiyoi SLIP is documented in studies by Xu et al. (2014), Shellnutt et al. (2011), Zhang and Zhang (2017), and Sato et al. (2015), respectively. The peak of volcanic activity is marked in dark green intervals. Data on global pCO₂ levels are drawn from the research conducted by Richey et al. (2020). Records of wildfire activity are referenced based on the abundance of inertinitite in the Yuzhou section and the Liujiang coalfield (Lu et al., 2021b; Wang et al., 2023). The corrected Chemical index of alteration (CIA*) was calculated for the Dacheng coalfield (Li et al., 2025). The eustatic curve for North China is based on the work of Lv et al. (2009). The $\delta^{18}\text{O}$ records from high-latitude regions are derived from Korte et al. (2008), while those from low-latitude areas are sourced from Korte et al. (2005). The extent of paleotropical forests is delineated by Cleal and Thomas (2005). The distribution patterns of coal and redbeds across North China are cited from Zhang et al. (1999) and Wang (2010). Floristic turnover in North China is documented by Stevens et al. (2011). On the plot, the first appearance of species (species gain, positive values) is shown on the left, while the last appearance within a stratigraphic bed (species loss, negative values) is displayed on the right, both accompanied by binomial 95 % confidence intervals (horizontal bars). The solid grey line depicts the mean species turnover, highlighting the shifts in the balance between species gain and loss. Below the floristic turnover curve, numerical values indicate the counts of species gained (positive) and lost (negative). The grey shaded area marks the extinction event recorded in the Lower Shihhotse Formation. The climate transitions recorded in Euramerica are based on the findings of Tabor and Poulsen (2008). The stratigraphic variations are detailed in Fig. 2. The age model is constrained by radiometric ages from tuffaceous mudstone samples (D11-7-TM1 and D11-7-TM2) within the Dacheng coalfield, and a CA-ID-TIMS age marking the top of the Taiyuan Formation in the Yongcheng coalfield (Yang et al., 2020). Numerical timescale after <http://www.stratigraphy.org/ICSchart/ChronostratChart2024-12>. (For interpretation of the references to colour in this figure legend, the reader is referred to the web version of this article.)

of the Cisuralian basalts (Wang et al., 2018a, 2018b). This volume is comparable to the thermal release of approximately 3000 Gt of gas from the Vøring and Møre basins of the Eocene North Atlantic Igneous Province (NAIP) (Svensen et al., 2004). Svensen et al. (2004) suggested that the release of 1100 Gt of methane could be sufficient to induce a

carbon isotope excursion of more than -2.5 ‰ during the Eocene thermal maximum. In the Dacheng coalfield, Hg and Hg/TOC peaks coinciding with negative $\delta^{13}\text{C}_{\text{org}}$ excursions during the late Sakmarian are stratigraphically constrained to the tuffaceous mudstone layer D11-7-TM1 ($290.7 \pm 3.3 \text{ Ma}$; Fig. 9), establishing a genetic linkage between

Hg anomalies and Tarim II LIP volcanism evidenced by this synchronous volcanic marker. Meanwhile, the tuffaceous layers exhibit concurrent peaks in Hg, Co, and Mo, elements consistently linked to large igneous province (LIP) emplacement (“LIP marks”; Grasby et al., 2015, 2019; Ostrander et al., 2017; Fig. 6). Crucially, this co-enrichment occurs while Ni and V remain stable with invariant V/(V + Ni) ratios (Fig. 6). This decoupling reflects that the stability of the redox-sensitive V/(V + Ni) ratio, which argues against a shift to sulfidic conditions that typically drive coupled V and Ni enrichment (Tribouillard et al., 2006; Qiao et al., 2016). Instead, it indicates persistently sub-euoxic conditions that limited Ni sequestration through sulfide fixation (Hatch and Leventhal, 1992). Consequently, the Hg-Co-Mo co-enrichment likely indicates direct volcanic inputs rather than redox-controlled enrichment processes. Furthermore, the lack of Ni concentration peaks during this interval may also originate from the absence of Ni-rich deposits intruded by the Tarim LIP magmas, preventing significant Ni-rich volatiles release. This contrasts with the Siberian Traps, where distinct Ni signals are linked to the interaction of magmas with Ni-rich deposits (Rampino et al., 2017; Fielding et al., 2019). By integrating elemental covariation, redox-stable indices, and magmatic provenance constraints, this multi-proxy framework definitively constrains dominant volcanic controls during the ~291 Ma event, reconciles muted response of Ni, and demonstrates that Hg-Ni decoupling reflects differential elemental responses to volcanism rather than volcanic quiescence.

Other potential mechanisms that can lead to Hg anomalies in sedimentary records (Grasby et al., 2019) include wildfires (Grasby et al., 2017; Wang et al., 2018a, 2018b; Them et al., 2019; Wang et al., 2023), the denudation of continental soil cover (Sephton et al., 2005; Them et al., 2017), the melting of permafrost (Majorowicz et al., 2014; Schuster et al., 2018), decreases in glacial coverage (de Lacerda et al., 2017), or local redox conditions and sediment diagenesis. In the Liujiang coalfield and Yuzhou section, Hg anomalies during the early Artinskian show a correlation with an increase in inertinite content, which is traditionally regarded as direct evidence for wildfires in North China (Lu et al., 2021b; Wang et al., 2023; Fig. 9). In the Dacheng coalfield, Hg anomalies in the late Sakmarian correspond to an increase in inertinite content in the Liujiang coalfield. The data imply that wildfires occurring in North China during the late Sakmarian to Artinskian may have made a substantial contribution to Hg signals. However, late Sakmarian wildfires tend to show negligible Co release and orders-of-magnitude lower Hg flux than LIP volcanism, indicating wildfires may play secondary role in Hg emissions at ~291 Ma. Meanwhile, the CIA values of the Dacheng coalfield show no significant increase during Hg concentration peaks (Li et al., 2025; Fig. 9). This suggests that the observed Hg anomalies are unlikely linked to continental weathering processes. The negligible correlation between the Hg and Al (Fig. 7A) may indicate the Hg is largely derived from volcanic gas deposition and not significantly influenced by terrigenous input. Moreover, the melting of permafrost, if present (Wang et al., 2023), likely occurred predominantly during the deglaciation phase following the P1 glaciation, occurring in the earliest stages of the Artinskian (Fielding et al., 2023). This mechanism is considered unlikely to have played a role in the enhanced release of Hg observed during the late Sakmarian, especially in the paleotropical realm.

Pre-291 Ma mercury peaks (293 and 292.2 Ma) exhibit distinct behavior, non-elevated Hg/TOC ratios indicate mercury accumulation dominated by organic matter adsorption under redox fluctuations. Although occasional Mo enrichments occur at certain horizons in specific interval, they lack corresponding Co signals and tuff layers (Fig. 6), while charcoal peaks remain decoupled from $\delta^{13}\text{C}_{\text{org}}$ excursions (Fig. 9). This fundamentally contrasts with the 291 Ma event, where coupled Hg/TOC enrichment, negative $\delta^{13}\text{C}_{\text{org}}$ shifts, and diagnostic volcanic markers, collectively establish volcanism as the driver of global carbon cycle perturbation. Earlier mercury peaks likely reflect localized depositional controls (Fig. 9).

5.3. The driving factors of $\delta^{13}\text{C}$ variations and associated paleoclimate and paleoenvironmental changes

There seems to be an antithetic relationship between the timing of major volcanic activity and Permian glaciation in eastern Australia (Fielding et al., 2023). This relationship suggests that volcanic activity might have led to an increase in surface air temperatures, potentially bringing about the cessation of glacial intervals (Fielding et al., 2023). Compared to other global climate proxies of the same era, including Hg, Hg/TOC, $\delta^{13}\text{C}_{\text{org}}$, $\delta^{13}\text{C}_{\text{carb}}$, $p\text{CO}_2$, oxygen isotopes ($\delta^{18}\text{O}$), and sea-level fluctuations, it seems likely that a global volcanic event, as evidenced by the Tarim II LIP (Xu et al., 2014), could have potentially triggered the nonglacial interval separating the P1 and P2 glaciations (Figs. 8 and 9).

The negative shift in $\delta^{13}\text{C}_{\text{carb}}$ and $\delta^{13}\text{C}_{\text{org}}$ across the Sakmarian-Artinskian transition could be attributed to the release of ^{13}C -depleted volcanogenic carbon dioxide, potentially exacerbated by magma interactions with carbon-rich sedimentary deposits (Figs. 8 and 9). Contemporaneous with the rise in atmospheric CO_2 concentrations (Montañez et al., 2007; Richey et al., 2020), evidence suggests that volcanism could have been one of the key factors contributing to the transition from glacial to nonglacial climatic conditions (Fig. 9). The melting of ice sheets during the Sakmarian-Artinskian transition released substantial volumes of ^{18}O -depleted freshwater into the ocean, which would account for the globally recorded negative $\delta^{18}\text{O}$ excursions (Korte et al., 2005, 2008; Fig. 9). It should be noted that this freshwater influx represents a direct response to contemporaneous climatic warming. Furthermore, this event was likely accompanied by a global rise in sea-level (Haq and Schutter, 2008; Lv et al., 2009; Fig. 9).

The sustained increase in atmospheric $p\text{CO}_2$ during this period may have been influenced by factors in addition to volcanic activity. The rise in atmospheric $p\text{CO}_2$ levels during the earliest Artinskian could also have been partially attributed to decreased extent of tropical coal-forming forests (Cleal and Thomas, 2005), progressive shift towards a more arid climate (Tabor and Poulsen, 2008), and intensified wildfire activity (Wang et al., 2023).

In North China, a marked reduction in coal deposits occurred from the Shansi Formation to the Lower Shihhotse Formation (Fig. 9; Zhang et al., 1999; Wang, 2010; Sun et al., 2022a). This decline likely stems from degradation of regional wetland plant communities (Wang, 1985, 1989; Geng and Hilton, 1999), which critically terminated major coal-forming periods. Correlating with this shift is a distinct change in mudstone colour, transitioning from predominantly grey in the Shansi Formation to purple-reddish in the Lower Shihhotse Formation (Figs. 2 and 3), accompanied by a terrestrial ecosystem collapse. This collapse manifested as a significant plant extinction event that occurred during the earliest Artinskian period (Figs. 2 and 9; Stevens et al., 2011; Wu et al., 2021). Furthermore, progressively increasing red beds within the Lower Shihhotse Formation signify climatic transition towards drier, more seasonal conditions that restricted flourishing plant communities. This floral transformation occurred gradually over an extended interval, characterized by stepwise biodiversity reduction rather than abrupt change (Figs. 2 and 9). Collectively, these patterns suggest that volcanic activity was not the primary driver of these floral transitions.

Substantial vegetation changes near the Sakmarian-Artinskian boundary have been documented across pan-tropical Euramerican and Cathaysian floral realms (Gastaldo et al., 1996). These shifts align with evidence of progressive aridification in terrestrial environments from Euramerican tropics to China and the Far East (Fig. 9; Tabor and Poulsen, 2008). Aridification diminished silicate weathering capacity for atmospheric $p\text{CO}_2$ sequestration, while reduced coverage of tropical coal forests further compromised carbon storage. Oxidation of organic matter from wetland drying is likely to have been an ongoing process, continuously releasing CO_2 into the atmosphere and resulting in more pronounced negative $\delta^{13}\text{C}$ values over the long term.

Increased wildfires in peatlands also released large amounts of ^{12}C -rich CO_2 into the atmosphere and caused negative $\delta^{13}\text{C}$ excursions.

However, quantifying these impacts remains challenging due to complexities in reconstructing paleo-wetland dynamics. Conversely, volcanic activity typically occurs episodically, with intensity surges causing transient atmospheric $p\text{CO}_2$ increases and pronounced negative $\delta^{13}\text{C}$ excursions. Disentangling contributions from volcanic activity, wetland drying, wildfires, and other variables to changes in $p\text{CO}_2$ and the negative shifts in $\delta^{13}\text{C}$ values is inherently complex. This complexity arises from the contributions from different carbon sources, the varying durations of the events, and the magnitude and shape of the negative $\delta^{13}\text{C}$ excursions (Vervoort et al., 2019), which still require further investigation for the Artinskian warming event. It is most likely that the escalating role of volcanic activity (Richey et al., 2020; Wu et al., 2021; Wang et al., 2023), in conjunction with factors such as wetland forest degradation, intensifying aridification (Richey et al., 2020), and increased wildfires (Wang et al., 2023) may be accountable for mitigating the effects of the P1 glaciation and for the sustained rise in $p\text{CO}_2$ levels during the earliest Artinskian.

6. Conclusions

- (1) Negative shifts in $\delta^{13}\text{C}_{\text{org}}$ values within the Dacheng coalfield correspond to $\delta^{13}\text{C}$ records from other sections across South China, eastern Australia, the USA, and Russia during the Sakmarian-Artinskian transition. This overall global synchronicity suggests a widespread negative $\delta^{13}\text{C}$ shift, most likely driven by the release of ^{12}C enriched greenhouse gases and associated global warming, albeit with some regional variations in responses to carbon cycle perturbations. The timing of these negative shifts in $\delta^{13}\text{C}$ is generally coincident with the demise of the P1 glaciation across most of Gondwanaland and the loss of wetlands within the tropical zones.
- (2) Late Sakmarian (~291 Ma) Hg and Hg/TOC anomalies, synchronously coupled with negative $\delta^{13}\text{C}_{\text{org}}$ excursions and aligned with dated tuffaceous layers, demonstrate that volcanic activity, evidenced by Hg-Co-Mo co-enrichment under invariant redox conditions, was the primary driver of mercury anomalies and carbon cycle perturbances, with wildfires acting as a secondary contributor.
- (3) A global volcanic episode, represented by the Tarim II LIP, likely played a role in triggering an increase in atmospheric $p\text{CO}_2$ concentrations during the Sakmarian-Artinskian transition, driving the negative $\delta^{13}\text{C}$ excursion and rapid climatic warming that terminated the P1 glaciation and initiated the nonglacial interval that separated the P1 and P2 glaciations.
- (4) Sustained increase in atmospheric $p\text{CO}_2$ levels during the earliest Artinskian could be additionally attributed to the contraction of peat-forming, tropical forested regions, a progressive climatic shift towards increased aridification, and intensified wildfire regimes.

Supplementary data to this article can be found online at <https://doi.org/10.1016/j.palaeo.2025.113255>.

CRediT authorship contribution statement

Yanan Li: Writing – original draft, Investigation, Funding acquisition, Conceptualization. **Longyi Shao:** Writing – review & editing, Supervision, Conceptualization. **Christopher R. Fielding:** Writing – review & editing, Investigation. **Tracy D. Frank:** Writing – review & editing, Methodology. **Zhaorui Ye:** Resources. **Jing Lu:** Supervision, Methodology. **Kuan Yang:** Visualization, Data curation. **Shuai Wang:** Project administration, Funding acquisition, Conceptualization.

Declaration of competing interest

The authors declare that they have no known competing financial

interests or personal relationships that could have appeared to influence the work reported in this paper.

Acknowledgements

This research was supported by the National Natural Science Foundation of China (Grant No. 42302205 and No.42002128), the Fundamental Research Funding Project of Liaoning Education Department (Grant No. LJJKM2Z022020692), and the Open Fund of State Key Laboratory of Coal Resources and Safe Mining (Grant No. SKLCRSM22KFA07 and No. SKLCRSM20KFA02).

Data availability

The authors confirm that all data necessary for supporting the scientific findings of this paper have been provided.

References

- Algeo, T.J., Maynard, J.B., 2004. Trace-element behavior and redox facies in core shales of Upper Pennsylvanian Kansas-type cycloths. *Chem. Geol.* 206, 289–318. <https://doi.org/10.1016/j.chemgeo.2003.12.009>.
- Algeo, T.J., Kuwahara, K., Sano, H., Bates, S., Lyons, T., Elswick, E., Hinnov, L., Ellwood, B., Moser, J., Maynard, J.B., 2011. Spatial variation in sediment fluxes, redox conditions, and productivity in the Permian-Triassic Panthalassic Ocean. *Palaeogeogr. Palaeoclimatol. Palaeoecol.* 308, 65–83. <https://doi.org/10.1016/j.palaeo.2010.07.007>.
- Amos, H.M., Jacob, D.J., Kocman, D., Horowitz, H.M., Zhang, Y.X., Dutkiewicz, S., Horvat, M., Corbitt, E.S., Krabbenhoft, D.P., Sunderland, E.M., 2014. Global biogeochemical implications of mercury discharges from rivers and sediment burial. *Environ. Sci. Technol.* 48 (16), 9514–9522. <https://doi.org/10.1021/es502134t>.
- Birgenheier, L.P., Frank, T.D., Fielding, C.R., Rygel, M.C., 2010. Coupled carbon isotopic and sedimentological records from the Permian system of eastern Australia reveal the response of atmospheric carbon dioxide to glacial growth and decay during the late Palaeozoic Ice Age. *Palaeogeogr. Palaeoclimatol. Palaeoecol.* 286 (3–4), 178–193. <https://doi.org/10.1016/j.palaeo.2010.01.008>.
- Blum, J.D., Sherman, L.S., Johnson, M.W., 2014. Mercury isotopes in earth and environmental sciences. *Annu. Rev. Earth Planet. Sci.* 42, 249–269.
- Breit, G.N., Wanty, R.B., 1991. Vanadinite accumulation in carbonaceous rocks: a review of geochemical controls during deposition and diagenesis. *Chem. Geol.* 91, 83–97. [https://doi.org/10.1016/0009-2541\(91\)90083-4](https://doi.org/10.1016/0009-2541(91)90083-4).
- Bryan, S.E., 2021. Environmental impact of silicic magmatism in large igneous province events. In: Ernst, R.R., Dickson, A.J., Bekker, A. (Eds.), Large Igneous Provinces: A Driver of Global Environmental and Biotic Changes. American Geophysical Union, Hoboken, pp. 133–151. <https://doi.org/10.1002/9781119507444.ch6>.
- Burgess, S.D., Bowring, S.A., 2015. High-precision geochronology confirms voluminous magmatism before, during, and after Earth's most severe extinction. *Sci. Adv.* 1 (7), e1500470. <https://doi.org/10.1126/sciadv.1500470>.
- Chen, J., Xu, Y.G., 2019. Establishing the link between Permian volcanism and biodiversity changes: insights from geochemical proxies. *Gondw. Res.* 75, 68–96. <https://doi.org/10.1016/j.gr.2019.04.008>.
- Chumakov, N.M., 1994. Evidence of late Permian glaciation in the Kolyma River Basin: a repercussion of the Gondwana glaciations in Northeast Asia? *Stratigr. Geol. Correl.* 2, 426–444.
- Cleal, C.J., Thomas, B.A., 2005. Palaeozoic tropical rainforests and their effect on global climates: is the past the key to the present? *Geobiology* 3 (1), 13–31. <https://doi.org/10.1111/j.1472-4669.2005.00043.x>.
- Crowell, J.C., 1978. Gondwanan glaciation, cycloths, continental positioning, and climate change. *Am. J. Sci.* 278 (10), 1345–1372. <https://doi.org/10.2475/ajs.278.10.1345>.
- de Lacerda, L.D., Turcq, B., Sifeddine, A., Cordeiro, R.C., 2017. Mercury accumulation rates in Caço Lake, NE Brazil during the past 20,000 years. *J. South Am. Earth Sci.* 77, 42–50. <https://doi.org/10.1016/j.jsames.2017.04.008>.
- Dean, W.E., Gardner, J.V., Piper, D.Z., 1997. Inorganic geochemical indicators of glacial-interglacial changes in productivity and anoxia on the California continental margin. *Geochim. Cosmochim. Acta* 61, 4507–4518. [https://doi.org/10.1016/S0016-7037\(97\)00237-8](https://doi.org/10.1016/S0016-7037(97)00237-8).
- Domack, E.W., Burkley, L.A., Domack, C.R., Banks, M.R., 1993. Facies analysis of glacial marine pebbly mudstones in the Tasmania Basin: implications for regional paleoclimates during the late Paleozoic. In: Findlay, R.H., Unrug, R., Banks, M.R., Vevers, J.J. (Eds.), Gondwana Eight: Assembly, Evolution and Dispersal. Proceedings of the eight Gondwana symposium. Hobart, Tasmania, Australia, pp. 471–484.
- Erickson, B.E., Helz, G.R., 2000. Molybdenum(VI) speciation in sulfidic waters: stability and lability of thiomolybdates. *Geochim. Cosmochim. Acta* 64, 1149–1158. [https://doi.org/10.1016/S0016-7037\(99\)00423-8](https://doi.org/10.1016/S0016-7037(99)00423-8).
- Eros, J.M., Montañez, I.P., Davydov, V.I., Osleger, D.A., Nemyrovska, T.I., Poletaev, V.I., Zhykalyak, M.V., 2012. Reply to the comment on “Sequence stratigraphy and onlap history of the Donets Basin, Ukraine: insight into Carboniferous icehouse dynamics”.

- Palaeogeogr. Palaeoclimatol. Palaeoecol. 363–364, 187–191. <https://doi.org/10.1016/j.palaeo.2012.09.013>.
- Faure, K., de Wit, M.J., Willis, J.P., 1995. Late Permian global coal hiatus linked to ^{13}C -depleted CO_2 flux into the atmosphere during the final consolidation of Pangea. *Geology* 23 (6), 507–510. [https://doi.org/10.1130/0091-7613\(1996\)024<0473:LPGCHL>2.3.CO;2](https://doi.org/10.1130/0091-7613(1996)024<0473:LPGCHL>2.3.CO;2).
- Fielding, C.R., Frank, T.D., Isbell, J.L., 2008. The late Paleozoic ice age – a review of current understanding and synthesis of global climate patterns. In: Fielding, C.R., Frank, T.D., Isbell, J.L. (Eds.), *Resolving the Late Paleozoic Ice Age in Time and Space*. Geol. Soc. Am. Spec. Pap., 441, pp. 343–354. [https://doi.org/10.1130/2008.2441\(24\)](https://doi.org/10.1130/2008.2441(24)).
- Fielding, C.R., Frank, T.D., McLoughlin, S., Vajda, V., Mays, C., Tevyaw, A.P., Winguth, A., Winguth, C., Nicoll, R.S., Bocking, M., Crowley, J.L., 2019. Age and pattern of the southern high-latitude continental end-Permian extinction constrained by multi-proxy analysis. *Nat. Commun.* 10, 385. <https://doi.org/10.1038/s41467-018-07934-z>.
- Fielding, C.R., Frank, T.D., Birgenheier, L.P., 2023. A revised, late Paleozoic glacial time-space framework for eastern Australia, and comparisons with other regions and events. *Earth Sci. Rev.* 236, 104263. <https://doi.org/10.1016/j.earscirev.2022.104263>.
- Frank, T.D., Birgenheier, L.P., Montañez, I.P., Fielding, C.R., Rygel, M.C., 2008. Late Paleozoic climate dynamics revealed by comparison of ice-proximal stratigraphic and ice-distal isotopic records. In: Fielding, C.R., Frank, T.D., Isbell, J.L. (Eds.), *Resolving the Late Paleozoic Ice Age in Time and Space*. Geol. Soc. Am. Spec. Pap., 441, pp. 331–342. [https://doi.org/10.1130/2008.2441\(23\)](https://doi.org/10.1130/2008.2441(23)).
- Frank, T.D., Shultz, A.I., Fielding, C.R., 2015. Acme and demise of the late Paleozoic ice age: a view from the southeastern margin of Gondwana. *Palaeogeogr. Palaeoclimatol. Palaeoecol.* 418, 176–192. <https://doi.org/10.1016/j.palaeo.2014.11.016>.
- Gastaldo, R.A., DiMichele, W.A., Pfefferkorn, H.W., 1996. Out of the icehouse into the greenhouse: a late Paleozoic analog for modern global vegetational change. *GSAToday* 6, 1–7.
- Geng, B.Y., Hilton, J., 1999. New coniferophyte ovulate structures from the Early Permian of China. *Bot. J. Linn. Soc.* 129 (2), 115–138. <https://doi.org/10.1111/j.1095-8339.1999.tb00495.x>.
- Goldberg, K., Humayun, M., 2010. The applicability of the Chemical Index of Alteration as a paleoceanographic indicator: an example from the Permian of the Paraná Basin, Brazil. *Palaeogeogr. Palaeoclimatol. Palaeoecol.* 293 (1–2), 175–183. <https://doi.org/10.1016/j.palaeo.2010.05.015>.
- Grasby, S.E., Samei, H., Beauchamp, B., Chen, Z.H., 2013. Mercury deposition through the Permo-Triassic Biotic Crisis. *Chem. Geol.* 351, 209–216. <https://doi.org/10.1016/j.chemgeo.2013.05.022>.
- Grasby, S.E., Beauchamp, B., Bond, D.P.G., Wignall, P.B., Talavera, C., Galloway, J.M., Piepjohn, K., Reinhardt, L., Blomeier, D., 2015. Progressive environmental deterioration in northwestern Pangea leading to the latest Permian extinction. *GSA Bull.* 127 (9–10), 1331–1347. <https://doi.org/10.1130/B31197.1>.
- Grasby, S.E., Shen, W.J., Yin, R.S., Gleason, J.D., Blum, J.D., Lepak, R.F., Hurley, J.P., Beauchamp, B., 2017. Isotopic signatures of mercury contamination in latest Permian oceans. *Geology* 45 (1), 55–58. <https://doi.org/10.1130/G38487.1>.
- Grasby, S.E., Them II, T.R., Chen, Z.H., Yin, R.S., Ardakanli, O.H., 2019. Mercury as a proxy for volcanic emissions in the geological record. *Earth Sci. Rev.* 196, 102880. <https://doi.org/10.1016/j.earscirev.2019.102880>.
- Griffis, N.P., Montañez, I.P., Mundil, R., Richey, J., Isbell, J., Fedorchuk, N., Linol, B., Iannuzzi, R., Vesely, F., Mottin, T., da Rosa, E., Keller, B., Yin, Q.Z., 2019. Coupled stratigraphic and U-Pb zircon age constraints on the late Paleozoic icehouse-to-greenhouse turnover in south-Central Gondwana. *Geology* 47 (12), 1146–1150. <https://doi.org/10.1130/G46740.1>.
- Griffis, N., Montañez, I., Mundil, R., Le Heron, D., Dietrich, P., Kettler, C., Linol, B., Mottin, T., Vesely, F., Iannuzzi, R., Huyskens, M., Yin, Q.Z., 2021. High-latitude ice and climate control on sediment supply across SW Gondwana during the late Carboniferous and early Permian. *GSA Bull.* 133 (9–10), 2113–2124. <https://doi.org/10.1130/B35852.1>.
- Gröcke, D.R., 2002. The carbon isotope composition of ancient CO_2 based on higher-plant organic matter. *Philos. Trans. R. Soc. Lond. A* 360 (1793), 633–658. <https://doi.org/10.1098/rsta.2001.0965>.
- Haq, B.U., Schutter, S.R., 2008. A chronology of Paleozoic Sea-level changes. *Science* 322 (5898), 64–68. <https://doi.org/10.1126/science.1161648>.
- Hatch, J.R., Leventhal, J.S., 1992. Relationship between inferred redox potential of the depositional environment and geochemistry of the Upper Pennsylvanian (Missourian) Stark shale member of the dennis limestone, Wabaunsee County, Kansas, USA. *Chem. Geol.* 99 (1–3), 65–82. [https://doi.org/10.1016/0009-2541\(92\)90031-Y](https://doi.org/10.1016/0009-2541(92)90031-Y).
- Hayes, J.M., Strauss, H., Kaufman, A.J., 1999. The abundance of ^{13}C in marine organic matter and isotopic fractionation in the global biogeochemical cycle of carbon during the past 800 Ma. *Chem. Geol.* 161 (1–3), 103–125. [https://doi.org/10.1016/S0009-2541\(99\)00083-2](https://doi.org/10.1016/S0009-2541(99)00083-2).
- Heckel, P.H., 1994. Evaluation of evidence for glacio-eustatic control over marine Pennsylvanian cycloths in North America and consideration of possible tectonic events. In: Dennison, J.M., Ettensohn, F.R. (Eds.), *Tectonic and Eustatic Controls on Sedimentary Cycles*. SEPM Concepts Sedimentol. Paleontol., 4, pp. 65–87.
- Helz, G.R., Miller, C.V., Charnock, J.M., Mosselmans, J.F.W., Patrick, R.A.D., Garner, C. D., Vaughan, D.J., 1996. Mechanisms of molybdenum removal from the sea and its concentration in black shales: EXAFS evidences. *Geochim. Cosmochim. Acta* 60, 3631–3642. [https://doi.org/10.1016/0016-7037\(96\)00195-0](https://doi.org/10.1016/0016-7037(96)00195-0).
- Heydari, E., Arzani, N., Hassanzadeh, J., 2008. Mantle plume: the invisible serial killer – application to the Permian-Triassic boundary mass extinction. *Palaeogeogr.*
- Palaeoclimatol. Palaeoecol. 264 (1–2), 147–162. <https://doi.org/10.1016/j.palaeo.2008.04.013>.
- Huerta-Díaz, M.A., Morse, J.W., 1992. Pyritisation of trace metals in anoxic marine sediments. *Geochim. Cosmochim. Acta* 56, 2681–2702. [https://doi.org/10.1016/0016-7037\(92\)90353-K](https://doi.org/10.1016/0016-7037(92)90353-K).
- Isbell, J.L., Miller, M.F., Wolfe, K.L., Lenaker, P.A., 2003. Timing of late Paleozoic glaciation in Gondwana: was glaciation responsible for the development of northern hemisphere cyclothems? In: Chan, M.A., Archer, A.W. (Eds.), *Extreme Depositional Environments: Mega End Members in Geologic Time*. Geol. Soc. Am. Spec. Pap., vol. 370, pp. 5–24.
- Isbell, J.L., Vesely, F.F., Rosa, E.L.M., Pauls, K.N., Fedorchuk, N.D., Ives, L.R.W., McNall, N.B., Litwin, S.A., Borucki, M.K., Malone, J.E., Kusick, A.R., 2021. Evaluation of physical and chemical proxies used to interpret past glaciations with a focus on the late Paleozoic Ice Age. *Earth Sci. Rev.* 221, 103756. <https://doi.org/10.1016/j.earscirev.2021.103756>.
- Ishikawa, T., Ueno, Y., Komiya, T., Sawaki, Y., Han, J., Shu, D.G., Li, Y., Maruyama, S., Yoshida, N., 2008. Carbon isotope chemostratigraphy of Precambrian/Cambrian boundary section in the three Gorge area, South China: prominent global-scale isotope excursions just before the Cambrian Explosion. *Gondw. Res.* 14 (1–2), 193–208. <https://doi.org/10.1016/j.gr.2007.10.008>.
- Isozaki, Y., Kawahata, H., Minoshima, K., 2007a. The Capitanian (Permian) Kamura cooling event: the beginning of the Paleozoic-Mesozoic transition. *Palaeoworld* 16 (1–3), 16–30. <https://doi.org/10.1016/j.palwov.2007.05.011>.
- Isozaki, Y., Kawahata, H., Ota, A., 2007b. A unique carbon isotope record across the Guadalupian-Lopingian (Middle–Upper Permian) boundary in mid-oceanic paleo-atoll carbonates: the high-productivity “Kamura event” and its collapse in Panthalassa. *Global Planet. Change* 55 (1–3), 21–38. <https://doi.org/10.1016/j.gloplacha.2006.06.006>.
- Javoy, M., Pineau, F., Delorme, H., 1986. Carbon and nitrogen isotopes in the mantle. *Chem. Geol.* 57 (1–2), 41–62. [https://doi.org/10.1016/0009-2541\(86\)90093-8](https://doi.org/10.1016/0009-2541(86)90093-8).
- Jones, M.T., Percival, L.M.E., Stokke, E.W., Frieling, J., Mather, T.A., Riber, L., Schubert, B.A., Schultz, B., Tegner, C., Planke, S., Svensen, H.H., 2019. Mercury anomalies across the Palaeocene-Eocene thermal maximum. *Clim. Past* 15, 217–236. <https://doi.org/10.5194/cp-15-217-2019>.
- Kaiho, K., Kajiwara, Y., Nakano, T., Miura, Y., Kawahata, H., Tazaki, K., Ueshima, M., Chen, Z.Q., Shi, G.R., 2001. End-Permian catastrophe by a bolide impact: evidence of a gigantic release of sulfur from the mantle. *Geology* 29 (9), 815–818.
- Koch, J.T., Frank, T.D., 2012. Imprint of the late Paleozoic Ice Age on stratigraphic and carbon isotopic patterns in marine carbonates of the Orogena Basin, New Mexico, USA. *Sedimentology* 59 (1), 291–318. <https://doi.org/10.1111/j.1365-3091.2011.01258.x>.
- Korte, C., Jasper, T., Kozur, H.W., Veizer, J., 2005. $\delta^{18}\text{O}$ and $\delta^{13}\text{C}$ of Permian brachiopods: a record of seawater evolution and continental glaciation. *Palaeogeogr. Palaeoclimatol. Palaeoecol.* 224 (4), 333–351. <https://doi.org/10.1016/j.palaeo.2005.03.015>.
- Korte, C., Jones, P.J., Brand, U., Mertmann, D., Veizer, J., 2008. Oxygen isotope values from high-latitudes: clues for Permian Sea-surface temperature gradients and late Palaeozoic deglaciation. *Palaeogeogr. Palaeoclimatol. Palaeoecol.* 269 (1–2), 1–16. <https://doi.org/10.1016/j.palaeo.2008.06.012>.
- Kump, L.R., Arthur, M.A., 1999. Interpreting carbon-isotope excursions: carbonates and organic matter. *Chem. Geol.* 161 (1–3), 181–198. [https://doi.org/10.1016/S0009-2541\(99\)00086-8](https://doi.org/10.1016/S0009-2541(99)00086-8).
- Le Guerroué, E., Cozzi, A., 2010. Veracity of Neoproterozoic negative C-isotope values: the termination of the Shuram negative excursion. *Gondw. Res.* 17 (4), 653–661. <https://doi.org/10.1016/j.gr.2009.11.002>.
- Li, Y.N., Shao, L.Y., Fielding, C.R., Wang, D.W., Mu, G.Y., 2021. Sequence stratigraphy, paleogeography, and coal accumulation in a lowland alluvial plain, coastal plain, and shallow-marine setting: Upper Carboniferous-Permian of the Anyang-Hebi coalfield, Henan Province, North China. *Palaeogeogr. Palaeoclimatol. Palaeoecol.* 567, 110287. <https://doi.org/10.1016/j.palaeo.2021.110287>.
- Li, Y.N., Shao, L.Y., Fielding, C.R., Frank, T.D., Wang, D.W., Mu, G.Y., Lu, J., 2023. The chemical index of alteration in Permo-Carboniferous strata in North China as an indicator of environmental and climate change throughout the late Paleozoic Ice Age. *Global Planet. Change* 221, 104035. <https://doi.org/10.1016/j.gloplacha.2023.104035>.
- Li, Y.N., Shao, L.Y., Fielding, C.R., Frank, T.D., Ye, Z.R., Lu, J., Yang, K., Wang, S., 2025. Continental weathering linked to climate warming at the Sakmarian to Artinskian transition. *Global Planet. Change* 254, 105025. <https://doi.org/10.1016/j.gloplacha.2023.105025>.
- Liu, C., Jarochowska, E., Du, Y.S., Vachard, D., Munnecke, A., 2017. Stratigraphical and $\delta^{13}\text{C}$ records of Permo-Carboniferous platform carbonates, South China: responses to late Paleozoic icehouse climate and icehouse-greenhouse transition. *Palaeogeogr. Palaeoclimatol. Palaeoecol.* 474, 113–129. <https://doi.org/10.1016/j.palaeo.2016.07.038>.
- Lu, J., Wang, Y., Yang, M.F., Shao, L.Y., Hilton, J., 2021a. Records of volcanism and organic carbon isotopic composition ($\delta^{13}\text{C}_{\text{org}}$) linked to changes in atmospheric $p\text{CO}_2$ and climate during the Pennsylvanian icehouse interval. *Chem. Geol.* 570, 120168. <https://doi.org/10.1016/j.chemgeo.2021.120168>.
- Lu, J., Zhou, K., Yang, M.F., Zhang, P.X., Shao, L.Y., Hilton, J., 2021b. Records of organic carbon isotopic composition ($\delta^{13}\text{C}_{\text{org}}$) and volcanism linked to changes in atmospheric $p\text{CO}_2$ and climate during the late Paleozoic Icehouse. *Global Planet. Change* 207, 103654. <https://doi.org/10.1016/j.gloplacha.2021.103654>.
- Lv, D.W., Li, Z.X., Liu, H.Y., Guo, J.B., Liu, B.B., Meng, Z.L., 2009. The sea-level change and its response to the late Paleozoic sequence stratigraphy in North China. *Geol. China* 36 (5), 1079–1086.

- Lv, D.W., Wang, L.J., Isbell, J.L., Lu, C.Y., Li, P.P., Wang, Y.J., Zhang, Z.H., 2022. Records of chemical weathering and volcanism linked to paleoclimate transition during the late Paleozoic Icehouse. *Global Planet. Change* 217, 103934. <https://doi.org/10.1016/j.gloplacha.2022.103934>.
- Lv, D.W., Zhao, Y.T., Steel, R.J., Jia, H.B., Raji, M., Zhang, Z.H., Ju, L., Gong, L.H., Wang, X.Y., 2025. Massive organic carbon burial in the North China Basin is a main contributor to peak Late Paleozoic Ice Age in early Asselian. *Earth. Planet. Sc. Lett.* 661, 119370. <https://doi.org/10.1016/j.epsl.2025.119370>.
- Ma, R., Yang, J.H., Wang, Y., Yan, J.X., Liu, J., 2023. Estimating the magnitude of early Permian relative sea-level changes in southern North China. *Global Planet. Change* 221, 104036. <https://doi.org/10.1016/j.gloplacha.2023.104036>.
- Majorowicz, J., Grasby, S.E., Safanda, J., Beauchamp, B., 2014. Gas hydrate contribution to late Permian global warming. *Earth Planet. Sci. Lett.* 393, 243–253. <https://doi.org/10.1016/j.epsl.2014.03.003>.
- Marchetti, L., Forte, G., Kutschcher, E., DiMichele, W.A., Lucas, S.G., Roghi, G., Juncal, M.A., Hartkopf-Fröder, C., Krainer, K., Morelli, C., Rochi, A., 2022. The Artinskian Warming Event: an Euramerican change in climate and the terrestrial biota during the early Permian. *Earth Sci. Rev.* 226, 103922. <https://doi.org/10.1016/j.earscirev.2022.103922>.
- Martino, R.L., 2004. Sequence stratigraphy of the Glenshaw Formation (Middle-late Pennsylvanian) in the central Appalachian Basin. In: Pashin, J.C., Gastaldo, R.A. (Eds.), *Sequence Stratigraphy, Paleoclimate, and Tectonics of Coal-Bearing Strata. AAPG Studies in Geology*, 51, pp. 1–28.
- McElwain, J.C., Wade-Murphy, J., Hesselbo, S.P., 2005. Changes in carbon dioxide during an oceanic anoxic event linked to intrusion into Gondwana coals. *Nature* 435, 479–482. <https://doi.org/10.1038/nature03618>.
- Metcalfe, I., Crowley, J.L., Nicoll, R.S., Schmitz, M., 2015. High-precision U-Pb CA-TIMS calibration of Middle Permian to Lower Triassic sequences, mass extinction and extreme climate-change in eastern Australian Gondwana. *Gondw. Res.* 28 (1), 61–81. <https://doi.org/10.1016/j.gr.2014.09.002>.
- Meyers, P.A., 1997. Organic geochemical proxies of paleoceanographic, paleolimnologic, and paleoclimatic processes. *Org. Geochem.* 27 (5–6), 213–250. [https://doi.org/10.1016/S0146-6380\(97\)00049-1](https://doi.org/10.1016/S0146-6380(97)00049-1).
- Miller, K.G., Komink, M.A., Browning, J.V., Wright, J.D., Mountain, G.S., Katz, M.E., Sugarman, P.J., Cramer, B.S., Christie-Blick, N., Pekar, S.F., 2005. The Phanerozoic record of global sea-level change. *Science* 310 (5752), 1293–1298. <https://doi.org/10.1126/science.1116412>.
- Montañez, I.P., Poulsen, C.J., 2013. The late Paleozoic ice age: an evolving paradigm. *Annu. Rev. Earth Planet. Sci.* 41, 629–656. <https://doi.org/10.1146/annurev.earth.031208.100118>.
- Montañez, I.P., Tabor, N.J., Niemeier, D., DiMichele, W.A., Frank, T.D., Fielding, C.R., Isbell, J.L., Birgenheier, L.P., Rygel, M.C., 2007. CO₂-forced climate and vegetation instability during late Paleozoic deglaciation. *Science* 315 (5808), 87–91. <https://doi.org/10.1126/science.1134207>.
- Nriagu, J., Becker, C., 2003. Volcanic emissions of mercury to the atmosphere: global and regional inventories. *Sci. Total Environ.* 304 (1–3), 3–12. [https://doi.org/10.1016/s0048-9697\(02\)00552-1](https://doi.org/10.1016/s0048-9697(02)00552-1).
- Oplustil, S., Schmitz, M., Cleal, C.J., Martinek, K., 2016. A review of the Middle-Late Pennsylvanian west European regional substages and floral biozones, and their correlation to the Geological Time Scale based on new U-Pb ages. *Earth Sci. Rev.* 154, 301–335. <https://doi.org/10.1016/j.earscirev.2016.01.004>.
- Ostrander, C.M., Owens, J.D., Nielsen, S.G., 2017. Constraining the rate of oceanic deoxygenation leading up to a Cretaceous Oceanic Anoxic Event (OAE-2: ~94 Ma). *Sci. Adv.* 3, e1701020. <https://doi.org/10.1126/sciadv.1701020>.
- Percival, L.M.E., Witt, M.L.I., Mather, T.A., Hermoso, M., Jenkyns, H.C., Hesselbo, S.P., Al-Suwaidi, A.H., Storm, M.S., Xu, W., Ruhl, M., 2015. Globally enhanced mercury deposition during the end-Pliensbachian extinction and Toarcian OAE: a link to the Karoo-Ferrar Large Igneous Province. *Earth Planet. Sci. Lett.* 428, 267–280. <https://doi.org/10.1016/j.epsl.2015.06.064>.
- Percival, L.M.E., Ruhl, M., Hesselbo, S.P., Jenkyns, H.C., Mather, T.A., Whiteside, J.H., 2017. Mercury evidence for pulsed volcanism during the end-Triassic mass extinction. *PNAS* 114 (30), 7929–7934. <https://doi.org/10.1073/pnas.1705378114>.
- Percival, L.M.E., Jenkyns, H.C., Mather, T.A., Dickson, A.J., Batenburg, S.J., Ruhl, M., Hesselbo, S.P., Barclay, R., Jarvis, I., Robinson, S.A., Woelders, L., 2018. Does large igneous province volcanism always perturb the mercury cycle? Comparing the records of oceanic anoxic event 2 and the end-Cretaceous to other Mesozoic events. *Am. J. Sci.* 318, 799–860. <https://doi.org/10.2475/08.2018.01>.
- Pyle, D.M., Mather, T.A., 2003. The importance of volcanic emissions for the global atmospheric mercury cycle. *Atmos. Environ.* 37 (36), 5115–5124. <https://doi.org/10.1016/j.atmosenv.2003.07.011>.
- Qiao, J.Q., Liu, L.F., Shang, X.Q., Li, B.Y., 2016. The relationship between V, Ni or V/Ni ratio and each of organic matter abundance and diagenetic evolution stages in shales: taking the shales in Fukang Sag of Junggar Basin for example. *Bull. Mineral. Petrol. Geochem.* 35 (4), 756–768. [https://doi.org/10.3969/j.issn.1028.2016.04.016. \(In Chinese with English abstract\)](https://doi.org/10.3969/j.issn.1028.2016.04.016).
- Rampino, M.R., Prokoph, A., Adler, A.C., Schwintdt, D.M., 2002. Abruptness of the end-Permian mass extinction as determined from biostratigraphic and cyclostratigraphic analyses of European western Tethyan sections. In: Koerber, C., MacLeod, K.G. (Eds.), *Catastrophic Events and Mass Extinctions: Impacts and Beyond. Geol. Soc. Am. Spec. Pap.*, vol. 356, pp. 415–427.
- Rampino, M.R., Rodriguez, S., Baransky, E., Cai, Y., 2017. Global nickel anomaly links Siberian Traps eruptions and the latest Permian mass extinction. *Sci. Rep.* 7, 12416. <https://doi.org/10.1038/s41598-017-12759-9>.
- Richey, J.D., Montañez, I.P., Goddérus, Y., Looy, C.V., Griffis, N.P., DiMichele, W.A., 2020. Influence of temporally varying weatherability on CO₂-climate coupling and ecosystem change in the late Paleozoic. *Clim. Past* 16 (5), 1759–1775. <https://doi.org/10.5194/cp-16-1759-2020>.
- Rosa, E.L.M., Isbell, J.L., 2021. Late paleozoic glaciation. In: Alderton, D., Elias, S.A. (Eds.), *Encyclopedia of Geology*, Second ed. Academic Press, Oxford, pp. 534–545. <https://doi.org/10.1016/B978-0-08-102908-4.00063-1>.
- Ross, C.A., Ross, J.R.P., 1987. Late Paleozoic Sea levels and depositional sequences. *Cushman Found. Foram. Res. Spec. Publ.* 24, 137–149.
- Rothman, D.H., Fournier, G.P., French, K.L., Alm, E.J., Boyle, E.A., Cao, C.Q., Summons, R.E., 2014. Methanogenic burst in the end-Permian carbon cycle. *PNAS* 111 (15), 5462–5467. <https://doi.org/10.1073/pnas.1318106111>.
- Rygel, M.C., Fielding, C.R., Frank, T.D., Birgenheier, L.P., 2008. The magnitude of late Paleozoic glacioeustatic fluctuations: a synthesis. *J. Sediment. Res.* 78 (8), 500–511. <https://doi.org/10.2110/jsr.2008.058>.
- Sanei, H., Grasby, S.E., Beauchamp, B., 2012. Latest Permian mercury anomalies. *Geology* 40 (1), 63–66. <https://doi.org/10.1130/G32596.1>.
- Sato, A.M., Llambías, E.J., Basei, M.A.S., Castro, C.E., 2015. Three stages in the late Paleozoic to Triassic magmatism of southwestern Gondwana, and the relationships with the volcanic events in coeval basins. *J. South Am. Earth Sci.* 63, 48–69. <https://doi.org/10.1016/j.james.2015.07.005>.
- Schuster, P.F., Schaefer, K.M., Aiken, G.R., Antweiler, R.C., Dewild, J.F., Gryziec, J.D., Gusmeroli, A., Hugelius, G., Jafarov, E., Krabbenhoft, D.P., Liu, L., Herman-Mercer, N., Mu, C.C., Roth, D.A., Schaefer, T., Striegl, R.G., Wickland, K.P., Zhang, T.J., 2018. Permafrost stores a globally significant amount of mercury. *Geophys. Res. Lett.* 45 (3), 1463–1471. <https://doi.org/10.1002/2017GL075571>.
- Scotese, C.R., 2014. Atlas of Permo-Triassic Paleogeographic Maps (Mollweide Projection), Map 43–52, Volumes 3&4 of the Paleomap Atlas for ArcGIS, Paleomap Project, Evanston, IL. Tech. Rep. <https://doi.org/10.13140/2.1.2609.9209>.
- Septon, M.A., Looy, C.V., Brinkhuis, H., Wignall, P.B., de Leeuw, J.W., Visscher, H., 2005. Catastrophic soil erosion during the end-Permian biotic crisis. *Geology* 33 (12), 941–944. <https://doi.org/10.1130/G21784.1>.
- Shao, L.Y., Dong, D.X., Li, M.P., Wang, D.D., Lu, J., Zheng, M.Q., Cheng, A.G., 2014. Sequence-paleogeography and coal accumulation of the Carboniferous-Permian in the North China Basin. *J. China Coal Soc.* 39 (8), 1725–1734. [https://doi.org/10.13225/j.cnki.jccs.2013.9033. \(In Chinese with English abstract\)](https://doi.org/10.13225/j.cnki.jccs.2013.9033. (In Chinese with English abstract)).
- Shao, Y.W., Zhao, F.H., Spiro, B., Li, D.H., Mu, G.Y., Chu, J.M., Lu, J., Shao, L.Y., 2024. Net primary productivity of paleo-peatlands linked to deep-time glacial periods in the late Carboniferous and early Permian icehouse interval. *Int. J. Coal Geol.* <https://doi.org/10.1016/j.coal.2024.104644> in press.
- Shellnutt, J.G., Bhat, G.M., Brookfield, M.E., Jahn, B.-M., 2011. No link between the Panjal Traps (Kashmir) and the Late Permian mass extinctions. *Geophys. Res. Lett.* 38, L19308. <https://doi.org/10.1029/2011GL049032>.
- Shen, S.Z., Zhang, H., Zhang, Y.C., Yuan, D.X., Chen, B., He, W.H., Mu, L., Lin, W., Wang, W.Q., Chen, J., Wu, Q., Cao, C.Q., Wang, Y., Wang, X.D., 2019. Permian integrative stratigraphy and timescale of China. *Sci. China. Earth Sci.* 62, 154–188. <https://doi.org/10.1007/s11430-017-9228-4>.
- Shen, B.H., Shen, S.Z., Wu, Q., Zhang, S.C., Zhang, B., Wang, X.D., Hou, Z.S., Yuan, D.X., Zhang, Y.C., Liu, F., Zhang, H., Shi, Y.K., Wang, J., Feng, Z., 2022a. Carboniferous and Permian integrative stratigraphy and timescale of North China Block. *Sci. China Earth Sci.* 65 (6), 983–1011. <https://doi.org/10.1007/s11430-021-9909-9>.
- Shen, J., Yin, R., Algeo, T.J., Svensen, H.H., Schoepfer, S.D., 2022b. Mercury evidence for combustion of organic-rich sediments during the end-Triassic crisis. *Nat. Commun.* 13 (1), 1–8. <https://doi.org/10.1038/s41467-022-28891-8>.
- Shen, J., Chen, J.B., Yu, J.X., Algeo, T.J., Smith, R.M.H., Botha, J., Frank, T.D., Fielding, C.R., Ward, P.D., Mather, T.A., 2023. Mercury evidence from southern Pangea terrestrial sections for end-Permian global volcanic effects. *Nat. Commun.* 14, 6. <https://doi.org/10.1038/s41467-022-35272-8>.
- Sial, A.N., Lacerda, L.D., Ferreira, V.P., Frei, R., Marquillas, R.A., Barbosa, J.A., Gaucher, C., Windmöller, C.C., Pereira, N.S., 2013. Mercury as a proxy for volcanic activity during extreme environmental turnover: the Cretaceous–Paleogene transition. *Palaeogeogr. Palaeoclimatol. Palaeoecol.* 387, 153–164. <https://doi.org/10.1016/j.palaeo.2013.07.019>.
- Soreghan, G.S., Soreghan, M.J., Heavens, N.G., 2019. Explosive volcanism as a key driver of the late Paleozoic ice age. *Geology* 47 (7), 600–604. <https://doi.org/10.1130/G46349.1>.
- Stevens, L.G., Hilton, J., Bond, D.P.G., Glasspool, I.J., Jardine, P.E., 2011. Radiation and extinction patterns in Permian floras from North China as indicators for environmental and climate change. *J. Geol. Soc. Lond.* 168 (2), 607–619. <https://doi.org/10.1144/0016-76492010-042>.
- Sun, S., Chen, A.Q., Chen, H.D., Hou, M.C., Yang, S., Xu, S.L., Wang, F., Huang, Z.F., Ogg, J.G., 2022a. Early Permian chemical weathering indices and paleoclimate transition linked to the end of the coal-forming episode, Ordos Basin, North China Craton. *Palaeogeogr. Palaeoclimatol. Palaeoecol.* 585, 110743. <https://doi.org/10.1016/j.palaeo.2021.110743>.
- Sun, F.N., Hu, W.X., Cao, J., Wang, X.L., Zhang, Z.R., Ramezani, J., Shen, S.Z., 2022b. Sustained and intensified lacustrine methane cycling during Early Permian climate warming. *Nat. Commun.* 13, 4856. <https://doi.org/10.1038/s41467-022-32438-2>.
- Svensen, H., Planke, S., Malthe-Sørensen, A., Jamtveit, B., Myklebust, R., Eidem, T.R., Rey, S.S., 2004. Release of methane from a volcanic basin as a mechanism for initial Eocene global warming. *Nature* 429, 542–545.
- Svensen, H., Planke, S., Polozov, A.G., Schmidbauer, N., Corfu, F., Podladchikov, Y.Y., Jamtveit, B., 2009. Siberian gas venting and the end-Permian environmental crisis. *Earth Planet. Sci. Lett.* 277 (3–4), 490–500. <https://doi.org/10.1016/j.epsl.2008.11.015>.
- Tabor, N.J., Poulsen, C.J., 2008. Palaeoclimate across the Late Pennsylvanian–Early Permian tropical palaeolatitudes: a review of climate indicators, their distribution,

- and relation to palaeophysiographic climate factors. *Palaeogeogr. Palaeoclimatol. Palaeoecol.* 268 (3–4), 293–310. <https://doi.org/10.1016/j.palaeo.2008.03.052>.
- Tang, H.S., Chen, Y.J., Wu, G., Lai, Y., 2011. Paleoproterozoic positive $\delta^{13}\text{C}_{\text{carb}}$ excursion in the northeastern Sino-Korean craton: evidence of the Lomagundi Event. *Gondwana Res.* 19, 471–481. <https://doi.org/10.1016/j.gr.2010.07.002>.
- Them, T.R., Gill, B.C., Selby, D., Gröcke, D.R., Friedman, R.M., Owens, J.D., 2017. Evidence for rapid weathering response to climatic warming during the Toarcian Oceanic Anoxic Event. *Sci. Rep.* 7, 5003. <https://doi.org/10.1038/s41598-017-05307-y>.
- Them, T.R., Jago, C.H., Caruthers, A.H., Gill, B.C., Grasby, S.E., Gröcke, D.R., Yin, R., Owens, J.D., 2019. Terrestrial sources as the primary delivery mechanism of mercury to the oceans across the Toarcian Oceanic Anoxic Event (Early Jurassic). *Earth Planet. Sci. Lett.* 507, 62–72. <https://doi.org/10.1016/j.epsl.2018.11.029>.
- Thibodeau, A.M., Ritterbush, K., Yager, J.A., West, A.J., Ibarra, Y., Bottjer, D.J., Berelson, W.M., Bergquist, B.A., Corsetti, F.A., 2016. Mercury anomalies and the timing of biotic recovery following the end-Triassic mass extinction. *Nat. Commun.* 7, 11147.
- Tierney, K.E., 2010. Carbon and Strontium Isotope Stratigraphy of the Permian from Nevada and China: Implications From an Icehouse to Greenhouse Transition. Doctoral dissertation. The Ohio State University, p. 168.
- Tribouillard, N., Algeo, T.J., Lyons, T., Riboulleau, A., 2006. Trace metals as paleoredox and paleoproductivity proxies: an update. *Chem. Geol.* 232 (1–2), 12–32. <https://doi.org/10.1016/j.chemgeo.2006.02.012>.
- Veevers, J.J., Powell, C.M.A., 1987. Late Paleozoic glacial episodes in Gondwanaland reflected in transgressive-regressive depositional sequences in Euramerica. *GSA Bull.* 98 (4), 475–487. [https://doi.org/10.1130/0016-7606\(1987\)98<475:LPGEIG>2.0.CO;2](https://doi.org/10.1130/0016-7606(1987)98<475:LPGEIG>2.0.CO;2).
- Vervoort, P., Adloff, M., Greene, S.E., Kirtland Turner, S., 2019. Negative carbon isotope excursions: an interpretive framework. *Environ. Res. Lett.* 14, 085014. <https://doi.org/10.1088/1748-9326/ab3318>.
- Wang, Z.Q., 1985. Palaeovegetation and plate tectonics: palaeophytogeography of North China during permian and triassic times. *Palaeogeogr. Palaeoclimatol. Palaeoecol.* 49 (1–2), 25–45. [https://doi.org/10.1016/0031-0182\(85\)90003-3](https://doi.org/10.1016/0031-0182(85)90003-3).
- Wang, Z.Q., 1989. Permian gigantic palaeobotanical events in North China. *Acta Palaeontol. Sin.* 28, 314–343.
- Wang, Z.Y., 1997. Chapter 3: multiple division of coal-bearing strata. In: Shang, G.X. (Ed.), Late Paleozoic Coal Geology Of North China Platform. Shanxi Science and Technology Publishing House, Taiyuan, Shanxi, pp. 13–82.
- Wang, J., 2010. Late Paleozoic macrofloral assemblages from Weihei Coalfield, with reference to vegetational change through the Late Paleozoic Ice-age in the North China Block. *Int. J. Coal Geol.* 83 (2–3), 292–317. <https://doi.org/10.1016/j.coal.2009.10.007>.
- Wang, L., Tian, W., Wei, Z.H., Gong, M.Y., Li, X.M., 2018a. Volcanic conduits of the Tarim Flood Basalt Province: 3D structure and thermogenic gas release. *Acta Petrol. Sinica* 34, 75–90 (in Chinese with English Abstract).
- Wang, X.D., Cawood, P.A., Zhao, H., Zhao, L.S., Grasby, S.E., Chen, Z.Q., Wignall, P.B., Lv, Z.Y., Han, C., 2018b. Mercury anomalies across the end Permian mass extinction in South China from shallow and deep water depositional environments. *Earth Planet. Sci. Lett.* 496, 159–167. <https://doi.org/10.1016/j.epsl.2018.05.04>.
- Wang, Y., Lu, J., Yang, M.F., Yager, J.A., Greene, S.E., Sun, R.Y., Mu, X.M., Bian, X., Zhang, P.X., Shao, L.Y., Hilton, J., 2023. Volcanism and wildfire associated with deep-time deglaciation during the Artinskian (early Permian). *Glob. Planet. Chang.* 225 (5), 104126. <https://doi.org/10.1016/j.gloplacha.2023.104126>.
- Wei, W., Algeo, T.J., 2020. Elemental proxies for paleosalinity analysis of ancient shales and mudrocks. *Geochim. Cosmochim. Acta.* 287, 341–366. <https://doi.org/10.1016/j.gca.2019.06.034>.
- Wu, Q., Ramezani, J., Zhang, H., Wang, J., Zeng, F.G., Zhang, Y.C., Liu, F., Chen, J., Cai, Y.F., Hou, Z.S., Liu, C., Yang, W., Henderson, C.M., Shen, S.Z., 2021. High-precision U-Pb age constraints on the Permian floral turnovers, paleoclimate change, and tectonics of the North China block. *Geology* 49 (6), 677–681. <https://doi.org/10.1130/G48051.1>.
- Xu, Y.G., Wei, X., Luo, Z.Y., Liu, H.Q., Cao, J., 2014. The Early Permian Tarim large Igneous Province: main characteristics and a plume incubation model. *Lithos* 204, 20–35. <https://doi.org/10.1016/j.lithos.2014.02.015>.
- Yager, J.A., West, A.J., Thibodeau, A.M., Corsetti, F.A., Rigo, M., Berelson, W.M., Bottjer, D.J., Greene, S.E., Ibarra, Y., Jadoul, F., Ritterbush, K.A., Rollins, N., Rosas, S., Di Stefano, P., Sulca, D., Todaro, S., Wynn, P., Zimmermann, L., Bergquist, B.A., 2021. Mercury contents and isotope ratios from diverse depositional environments across the Triassic–Jurassic Boundary: towards a more robust mercury proxy for large igneous province magmatism. *Earth-Sci. Rev.* 223, 103775. <https://doi.org/10.1016/j.earscirev.2021.103775>.
- Yang, J.H., Cawood, P.A., Du, Y.S., Feng, B., Yan, J.X., 2014. Global continental weathering trends across the Early Permian glacial to postglacial transition: correlating high- and low-paleolatitude sedimentary records. *Geology* 42 (10), 835–838. <https://doi.org/10.1130/G35892.1>.
- Yang, J.H., Cawood, P.A., Du, Y.S., Li, W.Q., Yan, J.X., 2016. Reconstructing early Permian tropical climates from chemical weathering indices. *GSA Bull.* 128, 739–751. <https://doi.org/10.1130/B31371.1>.
- Yang, J.H., Cawood, P.A., Montañez, I.P., Condon, D.J., Du, Y.S., Yan, J.X., Yan, S.Q., Yuan, D.X., 2020. Enhanced continental weathering and large igneous province induced climate warming at the Permo-Carboniferous transition. *Earth Planet. Sci. Lett.* 534, 116074. <https://doi.org/10.1016/j.epsl.2020.116074>.
- Zeng, J., Cao, C.Q., Davydov, V.I., Shen, S.Z., 2012. Carbon isotope chemostratigraphy and implications of palaeoclimatic changes during the Cisuralian (Early Permian) in the southern Urals, Russia. *Gondwana Res.* 21 (2–3), 601–610. <https://doi.org/10.1016/j.gr.2011.06.002>.
- Zhang, Z.X., 2014. Dacheng coalfield sedimentary environment of coal bearing strata. *Shandong Coal Sci. Technol.* 6, 147–148 (in Chinese with English Abstract).
- Zhang, Y.X., Zhang, K.J., 2017. Early Permian Qiangtang flood basalts, northern Tibet, China: a mantle plume that disintegrated northern Gondwana? *Gondwana Res.* 44, 96–108. <https://doi.org/10.1016/j.gr.2016.10.019>.
- Zhang, H., Shen, G.L., He, Z.L., 1999. Control of palaeoclimatic change on Late Paleozoic coal accumulation of the North China Plate. *Acta Geol. Sin.* 73 (2), 131–139.
- Zhang, S.H., Zhao, Y., Davis, G.A., Ye, H., Wu, F., 2014. Temporal and spatial variations of Mesozoic magmatism and deformation in the North China Craton: implications for lithospheric thinning and decratonization. *Earth-Sci. Rev.* 131, 49–87. <https://doi.org/10.1016/j.earscirev.2013.12.004>.
- Zhang, P.X., Yang, M.F., Lu, J., Bond, D.P.G., Zhou, K., Xu, X.T., Wang, Y., He, Z., Bian, X., Shao, L.Y., Hilton, J., 2023. End-Permian terrestrial ecosystem collapse in North China: evidence from palynology and geochemistry. *Glob. Planet. Chang.* 222, 104070. <https://doi.org/10.1016/j.gloplacha.2023.104070>.
- Zhang, W.J., Lin, S.M., Ke, X., Zhang, M., 2025. Composition characteristics and genesis of four types of high abundance rearranged hopanes in coal measure source rocks: a case study of Upper Paleozoic strata in the Ordos Basin. *Acta Sedimentol. Sin.* 43 (2), 683–700. <https://doi.org/10.14027/j.issn.1000-0550.2024.028>.
- Zhu, G.Y., Zhang, K.J., 2022. Did the eruption of the Tarim LIP control the formation of Paleozoic hydrocarbon reservoirs in the Tarim basin, China? *Gondwana Res.* 101, 224–232. <https://doi.org/10.1016/j.gr.2021.08.007>.
- Zhu, Z.Y., Jiang, S.Y., Liu, G.X., Zhao, K.D., 2013. Precise dating of the Middle Permian: zircon U-Pb geochronology from volcanic ash beds in the basal Gufeng Formation, Yangtze region, South China. *Gondwana Res.* 23 (4), 1599–1606. <https://doi.org/10.1016/j.gr.2012.08.008>.